LJMU Research Online

Zhang, S, Cyganowski, CJ, Henshaw, JD, Brogan, CL, Hunter, TR, Friesen, RK, Bonnell, IA and Viti, S

 Filamentary mass accretion towards the high-mass protobinary system G11.92-0.61 MM2

http://researchonline.ljmu.ac.uk/id/eprint/24257/

Article

Filamentary mass accretion towards the high-mass protobinary system G11.92−0.61 MM2

S. Zhang (张遂楠) [1,2]★ C. J. Cyganowski [1] J. D. Henshaw [3,4] C. L. Brogan [5] T. R. Hunter [5] R. K. Friesen [6] I. A. Bonnell[1] and S. Viti[7]

[1] *Scottish Universities Physics Alliance (SUPA), School of Physics and Astronomy, University of St Andrews, North Haugh, St Andrews KY16 9SS, UK*
[2] *Shanghai Astronomical Observatory, Chinese Academy of Sciences, 80 Nandan Road, Shanghai 200030, P. R. China*
[3] *Astrophysics Research Institute, Liverpool John Moores University, 146 Brownlow Hill, Liverpool L3 5RF, UK*
[4] *Max Planck Institute for Astronomy, Konigstuhl 17, D-69117 Heidelberg, Germany*
[5] *National Radio Astronomy Observatory, 520 Edgemont Road, Charlottesville, VA 22903, USA*
[6] *David A. Dunlap Department of Astronomy & Astrophysics, University of Toronto, 50 St. George St., Toronto ON M5S 3H4, Canada*
[7] *Leiden Observatory, Leiden University, P.O. Box 9513, NL-2300 RA Leiden, the Netherlands*

ABSTRACT

We present deep, sub-arcsecond ($\sim$2000 au) resolution ALMA 0.82-mm observations of the former high-mass prestellar core candidate G11.92–0.61 MM2, recently shown to be an $\sim$500 au-separation protobinary. Our observations show that G11.92–0.61 MM2, located in the G11.92–0.61 protocluster, lies on a filamentary structure traced by 0.82-mm continuum and N_2H^+(4-3) emission. The N_2H^+(4-3) spectra are multipeaked, indicative of multiple velocity components along the line of sight. To analyse the gas kinematics, we performed pixel-by-pixel Gaussian decomposition of the N_2H^+ spectra using SCOUSEPY and hierarchical clustering of the extracted velocity components using ACORNS. Seventy velocity- and position-coherent clusters (called 'trees') are identified in the N_2H^+-emitting gas, with the eight largest trees accounting for >60 per cent of the fitted velocity components. The primary tree, with $\sim$20 per cent of the fitted velocity components, displays a roughly north–south velocity gradient along the filamentary structure traced by the 0.82-mm continuum. Analysing an $\sim$0.17 pc-long substructure, we interpret its velocity gradient of $\sim$10.5 km s^{-1} pc^{-1} as tracing filamentary accretion towards MM2 and estimate a mass inflow rate of $\sim 1.8 \times 10^{-4}$ to 1.2×10^{-3} M$_\odot$ yr^{-1}. Based on the recent detection of a bipolar molecular outflow associated with MM2, accretion on to the protobinary is ongoing, likely fed by the larger scale filamentary accretion flows. If 50 per cent of the filamentary inflow reaches the protostars, each member of the protobinary would attain a mass of 8 M$_\odot$ within $\sim 1.6 \times 10^5$ yr, comparable to the combined time-scale of the 70-μm- and mid-infrared-weak phases derived for ATLASGAL-TOP100 massive clumps using chemical clocks.

Key words: stars: formation – stars: protostars – ISM: kinematics and dynamics – ISM: molecules.

1 INTRODUCTION

How mass aggregation proceeds during the formation of high-mass stars ($M_{ZAMS} \geq 8$ M$_\odot$) is a key open question in studies of star formation and the interstellar medium (ISM). In particular, whether and how the large-scale ($\gtrsim 1$ pc) environments of young high-mass stars affect their mass collection remains unclear: from what spatial scales do high-mass stars assemble their masses? How does the scale of the gas reservoir impact the final stellar mass of a high-mass star?

Core accretion models (e.g. McKee & Tan 2002, 2003) propose that the earliest phase of high-mass star formation is the high-mass prestellar core: a massive, gravitationally bound, centrally condensed, starless core with a radius ≤0.1 pc. High-mass prestellar cores are predicted to be self-contained gas reservoirs nearly in internal virial equilibrium, and initially in pressure equilibrium with their environment; they are then expected to undergo relatively ordered collapse to form single high-mass stars or small multiple systems (see the review of Tan et al. 2014, and references therein). However, cores with masses larger than the critical mass (i.e. the Jeans mass) are expected to fragment (e.g. Dobbs, Bonnell & Clark 2005). It thus remains a challenge for the core accretion theory to explain how a high-mass prestellar core (with $\sim 10^2$ Jeans masses) is supported against fragmentation (Tan et al. 2014).

Many numerical simulations have been carried out of the collapse of massive prestellar cores, both with and without magnetic fields. Radiation hydrodynamic simulations have demonstrated that the radiation pressure barrier problem can be overcome by disc accretion and flashlight effects due to outflow cavities (e.g. Krumholz et al. 2009; Cunningham et al. 2011; Kuiper, Yorke & Turner 2015; Rosen et al. 2019), with gas channelled to the star–disc system by gravitational and Rayleigh–Taylor instabilities (e.g. Krumholz et al. 2009, Rosen et al. 2016). Radiation magnetohydrodynamic (RMHD) simulations (e.g. Commerçon, Hennebelle & Henning 2011; Myers

★ E-mail: suinan.zhang@gmail.com

et al. 2013; Rosen & Krumholz 2020; Mignon-Risse, González & Commerçon 2021) have shown that the combined effects of magnetic fields and radiation can effectively suppress the initial fragmentation of massive dense cores by increasing the magnetic and thermal Jeans mass of the collapsing gas, contributing to the formation of massive stars. Recent RMHD simulations of the collapse of massive prestellar cores ($M = 150\,M_\odot$, $r = 0.1$ pc) including isotropic stellar winds show that accretion on to massive protostars with masses $\geq 30\,M_\odot$ is impeded by their wind feedback, suggesting that larger scale dynamical effects are required to form $> 30\,M_\odot$ stars (Rosen 2022).

Searching for high-mass prestellar cores in observations has, however, identified very few candidates in the past decades. Many initially promising candidates have been ruled out by subsequent observations that revealed signs of active star formation and/or resolved low-mass cores. G028C1-S, initially discovered to contain $\sim 60\,M_\odot$ within ~ 0.09 pc by Tan et al. (2013), has been resolved into two protostars driving outflows (Tan et al. 2016). Kong et al. (2017) reveal that G028C9A ($\sim 80\,M_\odot$ within ~ 0.05 pc) actually consists of two lower mass cores. In addition, though identified as one of the best high-mass prestellar core candidates ($\sim 25\,M_\odot$ within ~ 0.025 pc, Bontemps et al. 2010), CygXN53–MM2 is located close to CygXN53–MM1, a protostar driving outflows, making it difficult to distinguish if CygXN53–MM2 is not associated with any outflow (Duarte-Cabral et al. 2013, 2014). The most promising high-mass prestellar core candidates identified to date are G11P6-SMA1 ($\sim 30\,M_\odot$ within ~ 0.02 pc, Wang et al. 2014), W43-MM1 core 6 ($\sim 37\,M_\odot$, ~ 1800 au, Nony et al. 2018; Molet et al. 2019), AG354 ($\sim 39\,M_\odot$, Redaelli et al. 2021), and G028.37+00.07 C2c1a (~ 23–$31\,M_\odot$, Barnes et al. 2023)

In contrast, in competitive accretion models (e.g. Bonnell et al. 2001; Bonnell, Bate & Vine 2003) high-mass star formation is closely connected to cluster formation (e.g. Bonnell, Vine & Bate 2004). The fragmentation of turbulent molecular clouds produces low-mass cores as seeds of protostars (Bonnell et al. 2003). Protostars that are located near the centres of protoclusters are more likely to become massive stars, as these protostars have the advantage in being fed by gas infalling into the large-scale gravitational potential well of the cluster (e.g. Bonnell & Bate 2006). In this picture, the precursors of massive stars are predicted to accrete gas widely from their large-scale environments, in which case self-contained gas reservoirs (i.e. high-mass prestellar cores) do not necessarily exist. In numerical simulations spanning a range of initial conditions – from idealized spheres or cylinders of turbulent molecular clouds (e.g. Bonnell et al. 2004; Bonnell, Clark & Bate 2008; Smith, Longmore & Bonnell 2009; Maschberger et al. 2010) to more realistic spiral arm dynamics (e.g. Bonnell, Dobbs & Smith 2013; Smilgys & Bonnell 2016, 2017) – and included physics (such as photoionization, e.g. Dale & Bonnell 2011; Dale, Ercolano & Bonnell 2012, and photoionization plus radiation forces, e.g. Kuiper & Hosokawa 2018), high-mass stars form via significant accretion from $r \gtrsim 0.2$–10 pc spatial scales. More recently, by considering supernova-driven turbulence in magnetohydrodynamic (MHD) simulations of Giant Molecular Clouds (GMCs), Padoan et al. (2020) found that massive stars accumulate mass via inertial gas flows from parsec-scale filaments. Additionally, simulations of GMCs formed by supersonic convergent flows of warm diffuse atomic gas have led to the development of the global hierarchical collapse (GHC) scenario, in which multiscale collapse takes place within GMCs and (sub)structures at all scales (i.e. clouds, clumps, and cores) accrete from their larger scale environments via non-isotropic gas inflows (e.g. Vázquez-Semadeni et al. 2007, 2019; Gómez & Vázquez-Semadeni 2014; Vázquez-Semadeni, González-Samaniego & Colín 2017).

Many studies of the accretion reservoirs of forming high-mass stars have focused on infrared dark clouds (IRDCs), identified as extinction features against the Galactic mid-infrared (MIR) background (Butler & Tan 2009, 2012). IRDCs have been found to harbour the early phases of high-mass star and cluster formation (e.g. Rathborne, Jackson & Simon 2006; Jackson et al. 2010; Kauffmann & Pillai 2010; Peretto & Fuller 2010; Miettinen 2012a, b; Ragan et al. 2012; Busquet et al. 2013; Henshaw et al. 2013; Kainulainen et al. 2013; Peretto et al. 2013). They often display filamentary morphologies (e.g. Jackson et al. 2010; Henshaw et al. 2013; Beuther et al. 2015; André et al. 2016), with kinematic features of dense gas in IRDCs indicating gas flows along filaments (e.g. Zernickel, Schilke & Smith 2013; Henshaw et al. 2014; Tackenberg et al. 2014; Zhang et al. 2015; Chen et al. 2019). Multiple filaments can merge near the centre of a molecular cloud to form a hub, a phenomenon referred to as a 'hub-filament system' (e.g. Myers 2009; Hennemann et al. 2012; Schneider et al. 2012). Observations over the past decade have pointed to hub-filament systems playing a key role in shaping high-mass star and cluster formation (e.g. Peretto et al. 2013, 2014; Dewangan, Ojha & Baug 2017; Henshaw et al. 2017; Tigé et al. 2017; Hacar et al. 2018; Williams et al. 2018; Yuan et al. 2018; Chen et al. 2019; Keown et al. 2019; Treviño-Morales et al. 2019; Dewangan et al. 2020, Kumar et al. 2020, Wang et al. 2020, Anderson et al. 2021; Liu et al. 2023; Mookerjea et al. 2023; Zhou et al. 2023), with recent kinematic studies suggesting that hub-filament systems serve as the parsec-scale gas reservoirs feeding embedded young stars via filamentary gas flows (e.g. Zhou et al. 2022; Xu et al. 2023).

To investigate the properties of a candidate high-mass prestellar core and its relationship to its environment, we proposed ALMA Cycle 3–5 observations of G11.92–0.61 MM2 targeting $H_2D^+(1_{1,0}-1_{1,1})$ and $N_2H^+(4-3)$, which trace dense and depleted gas (Ceccarelli et al. 2014) and are commonly observed towards low-mass prestellar cores (Caselli et al. 2003; 2008; van der Tak, Caselli & Ceccarelli 2005; Vastel et al. 2006; Friesen et al. 2014; Koumpia et al. 2020; Miettinen 2020; Redaelli et al. 2021, 2022; Kong et al. 2023). G11.92–0.61 MM2 (hereafter MM2) is one of three massive millimetre cores associated with the GLIMPSE Extended Green Object (EGO; Cyganowski et al. 2008) G11.92−0.61, which were first detected with the Submillimeter Array (SMA) and the Combined Array for Research in Millimetre-wave Astronomy by Cyganowski et al. (2011a). Subsequent ALMA observations revealed 16 additional low-mass cores and showed that the G11.92−0.61 protocluster hosts ongoing, simultaneous high- and low-mass star formation (Cyganowski et al. 2017). MM2 is the second brightest mm source in the G11.92−0.61 protocluster. The brightest, MM1, has been resolved into a Keplerian disc around a proto-O star that is forming a binary system via disc fragmentation (Ilee et al. 2016, 2018).

Located ~ 0.12 pc from MM1, MM2 was considered to be a promising high-mass prestellar core candidate because it was a strong and compact dust continuum source that had no molecular line emission or other star formation indicators in SMA and VLA observations (Cyganowski et al. 2014, and references therein). In addition to its remarkable lack of (sub)mm line emission (no lines detected across ~ 24 GHz of bandwidth observed with the SMA at 1.3, 1.1, and 0.8 mm; Cyganowski et al. 2014), no CH_3OH or H_2O masers, molecular outflows, or cm continuum emission indicative of ionized gas had been detected in VLA and SMA imaging covering the G11.92−0.61 region (Hofner & Churchwell 1996; Cyganowski et al. 2009, 2011a, b, 2014; Breen & Ellingsen 2011; Hunter et al. 2015). The physical properties inferred by Cyganowski et al. (2014) based on their SMA and VLA data were extreme: $M \gtrsim 30\,M_\odot$ within

$R < 1000$ au and $n_{H_2} > 10^9$ cm^{-3}, with $T_{dust} \sim 17$–19 K and $L \sim 5$–7 $L_\odot$ from submillimeter SED fitting. Based on gas-grain astrochemical modelling using MONACO (Vasyunin et al. 2009), Cyganowski et al. (2014) found that the lack of line emission observed with the SMA could be explained with standard chemistry under cold ($T_{dust} < 20$ K) and very dense ($n_{H_2} \gg 10^8$ cm^{-3}) conditions. Deuterium fractionation is expected to take place at < 20 K, increasing the abundance of H_2D^+ (e.g. Caselli & Ceccarelli 2012; Redaelli et al. 2021). With most C- and O-bearing species frozen out on to dust grain surfaces, N_2H^+ becomes abundant as this molecule forms from the protonation of N_2 in cold environments and is destroyed mainly by reactions with CO (e.g. Öberg et al. 2005; van't Hoff et al. 2017). The expectation of extreme depletion motivated our targeting $H_2D^+(1_{1,0}-1_{1,1})$ and $N_2H^+(4\text{-}3)$ in our ALMA Band 7 observations.

Recent high-resolution ($\lesssim 160$ au) ALMA 1.3-mm observations targeting MM1 have changed the picture of MM2, revealing that MM2 is in fact a 505 au-separation protobinary system (Cyganowski et al. 2022). The members of the protobinary have 1.3-mm brightness temperatures of 68.4 and 64.6 K, indicative of internal heating; thus, MM2 is not a high-mass prestellar core but rather hosts the very early stages of high-mass binary formation (Cyganowski et al. 2022). Intriguingly, the discovery of a low-velocity asymmetric bipolar molecular outflow associated with MM2 in our deep ALMA Band 7 observations (traced by CH_3OH ($4_{-1,3}-3_{0,3}$), reported in Cyganowski et al. 2022) indicates that accretion on to the protobinary system is ongoing.

In this paper, we present our ALMA Band 7 continuum, H_2D^+ and N_2H^+ observations towards MM2, with a focus on the gas kinematics around MM2 traced by the N_2H^+ (4-3) emission. In Section 2, we provide details of the observations. In Section 3, we show the results for the dust continuum and molecular line emission. In Section 4, we describe the procedure used to perform Gaussian decomposition on the N_2H^+ data cube and in Section 5, we describe the hierarchical clustering analysis. Section 6 presents our analysis of the physical properties of the filamentary accretion flows, which are further discussed in Section 7. Section 8 summarizes our main conclusions. Throughout this work, we assume that MM2 is located at the same distance as MM1 and adopt MM1's maser parallax distance of $3.37^{+0.39}_{-0.32}$ kpc (Sato et al. 2014).

2 ALMA OBSERVATIONS

We observed MM2 at 0.82 mm with the ALMA 12-m array in Cycles 3–5 (project codes 2015.1.00827.S and 2017.1.01373.S, PI C. Cyganowski). The phase centre of the single-pointing observations was $18^h13^m57^s.8599$ $-18°54'13''.958$ (ICRS); at 0.82 mm, the full width half-power (FWHP) size of the primary beam is $\sim 17''$ (see Fig. 1). Additional observational parameters, including observing dates, configurations, and calibrators, are listed in Table 1. The projected baselines of the combined data set range from ~ 14–583 kλ, corresponding to a largest angular scale (LAS)[1] of ~ 4.5 arcsec (~ 0.07 pc $\sim 15\,200$ au at $D = 3.37$ kpc).

The correlator setup included four spectral windows (spws): three narrow spws tuned to cover $H_2D^+(1_{1,0}-1_{1,1})$ ($\nu_{rest} = 372.421$ GHz, $E_{upper} = 104.2$ K), $N_2H^+(4\text{-}3)$ ($\nu_{rest} = 372.672$ GHz, $E_{upper} = 44.7$ K), and $DCO^+(5\text{-}4)$
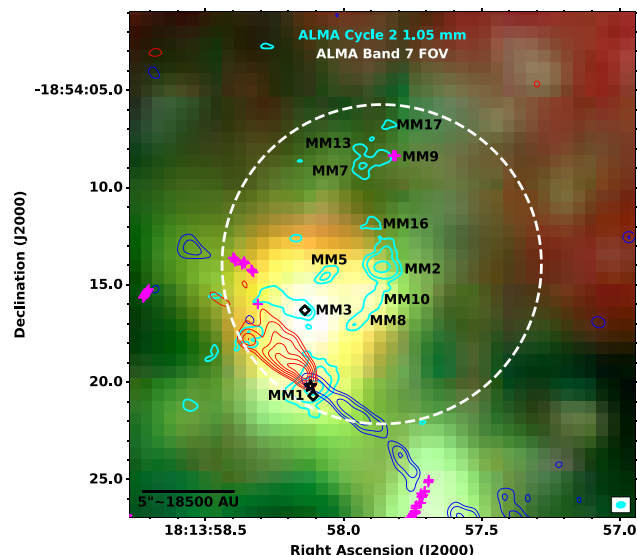
Figure 1. *Spitzer* GLIMPSE three-colour image (red 8.0 μm, green 4.5 μm, and blue 3.6 μm) overlaid with contours of the ALMA Cycle 2 1.05-mm continuum emission (cyan: [5, 15, 100] $\times$ 0.35 mJy beam^{-1}, Cyganowski et al. 2017) and SMA blueshifted and redshifted ^{12}CO (3-2) line emission (blue: [4, 6, 9] $\times$ 1.0 Jy km s^{-1}, red: [4, 6, 9, 12, 15, 18] $\times$ 1.0 Jy km s^{-1}, Cyganowski et al. 2014, 2017). The magenta $+$ and black $\diamond$ mark the locations of Class I and Class II CH_3OH masers, respectively, from Cyganowski et al. (2009) and the black star in MM1 marks the H_2O maser from Breen & Ellingsen (2011). The dashed white circle indicates the 50 per cent response level of the primary beam for our ALMA Band 7 observations. The synthesized beam of the ALMA Cycle 2 1.05-mm continuum image is shown at bottom right.

($\nu_{rest} = 360.170$ GHz, $E_{upper} = 51.9$ K),[2] and a wide spw, centred at ~ 358.02 GHz, for continuum sensitivity. The observed bandwidths and spectral resolutions (accounting for online Hanning smoothing and channel averaging) were 117.2 MHz (~ 94 km s^{-1}) and 0.122 MHz (~ 0.098 km s^{-1}) for H_2D^+, 58.6 MHz (~ 47 km s^{-1}) and 0.061 MHz (~ 0.049 km s^{-1}) for N_2H^+, 243.4 MHz (~ 195 km s^{-1}) and 0.141 MHz (~ 0.117 km s^{-1}) for DCO^+, and 1875 MHz (~ 1570 km s^{-1}) and 1.129 MHz (~ 0.945 km s^{-1}) for the wide spw.

The data were calibrated using the CASA 5.4.0 version of the ALMA science pipeline. Line-free channels were identified using the approach of Brogan et al. (2016) and Cyganowski et al. (2017) and used to construct a pseudo-continuum data set, which has an aggregate continuum bandwidth of ~ 0.44 GHz. These continuum data were iteratively self-calibrated, and the solutions were then applied to the line data. The final continuum image, made using multifrequency synthesis, multiscale clean, and Briggs weighting with a robust parameter $R = 0.5$, has an rms noise level of $1\sigma = 0.5$ mJy beam^{-1} and a synthesized beam size of $0.575'' \times 0.431''$ (PA $= -80°$), equivalent to $\sim 1940 \times 1450$ au^2 at $D = 3.37$ kpc. In this paper, we consider only the continuum, N_2H^+, and H_2D^+ data; images of the CH_3OH ($4_{-1,3}\text{-}3_{0,3}$) line, included in the wide spw, were presented in Cyganowski et al. (2022) (see also Section 1). The N_2H^+ line data were imaged with multiscale clean, Briggs weighting with a robust parameter $R = 0.5$, and a velocity resolution $\Delta v = 0.2$ km s^{-1}. The resulting N_2H^+ (4-3) image cube has a synthesized beam size of $0.651'' \times 0.442''$ (PA $= -79°$) and an rms noise level of

---

[1]Estimated from the fifth percentile shortest baseline using the ANALYSISU-TILS (Hunter et al. 2023) task au.estimateMRS.

[2]Line rest frequencies are from CDMS (Müller et al. 2001, 2005), accessed via the Splatalogue NRAO spectral line catalogue (https://splatalogue.online/).

Table 1. Summary of ALMA 0.82-mm observations.

Project code	Observing date	Configuration	Number of antennas	Time on-source		Calibrators	
					Gain	Bandpass	Flux
2015.1.00827.S	2016 April 9[a]	C36-2/3	43	2×42.5 min	J1733–1304	J1924–2914	J1924-2914, Titan
2015.1.00827.S	2017 April 22	C40-3	41	42.5 min	J1733–1304	J1924–2914	Titan
2015.1.00827.S	2017 April 26	C40-3	41	42.5 min	J1733–1304	J1924–2914	Titan
2017.1.01373.S	2018 July 10	C43-1	46	46.5 min	J1911–2006	J1924–2914	J1924–2914
2017.1.01373.S	2018 August 16	C43-2	43–44	3×46.5 min	J1911–2006	J1924–2914	J1924–2914

[a]Due to a tuning issue, the correlator setup on this date did not cover N_2H^+ (4-3).
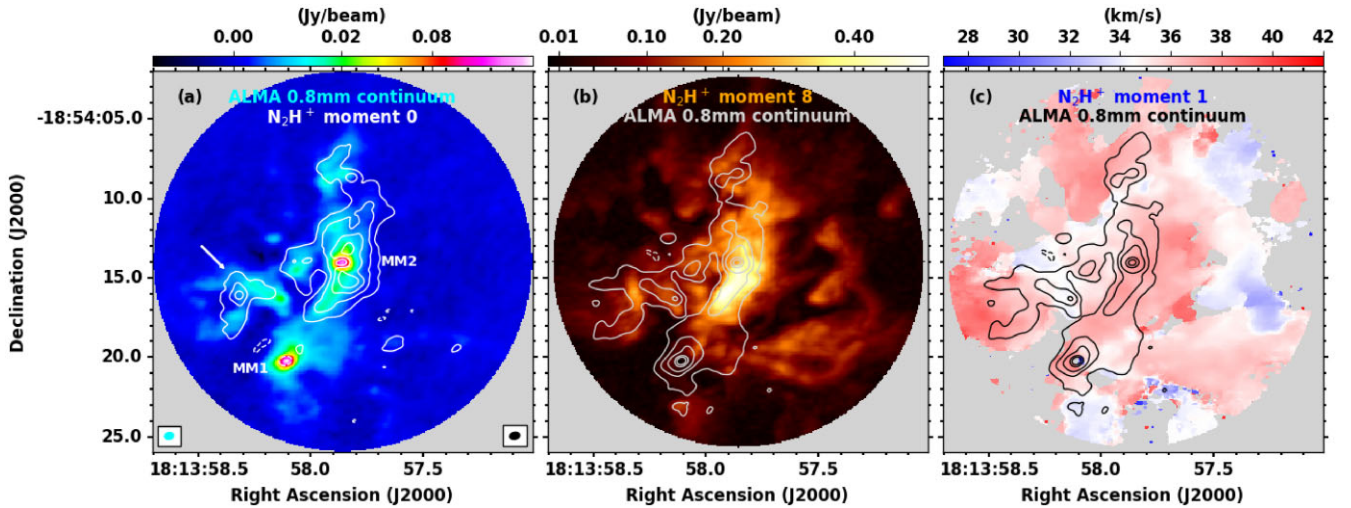
Figure 2. Panel (a): ALMA 0.82 mm continuum (colour scale) overlaid with contours of integrated N_2H^+(4-3) emission (velocity range: 27.0–42.0 km s^{-1}; levels: 0.06 Jy km s$^{-1}\times$ [–2, 5, 10, 15, 20], negative contours shown as dashed lines). The arrow marks the bow-like feature discussed in Section 3.2.2 and the synthesized beams of the 0.82 mm continuum image and N_2H^+ cube are shown at bottom left (in cyan) and right (in black), respectively. Panel (b): ALMA N_2H^+ peak intensity map (colour scale) overlaid with 0.82-mm continuum contours. Panel (c): N_2H^+(4-3) moment 1 map (colour scale) overlaid with 0.82-mm continuum contours. In the moment 1 map, pixels with line emission $<4 \times \sigma_{npb}$, where $\sigma_{npb} = 4.7$mJy beam^{-1} is the rms of the N_2H^+ cube before primary beam correction, are masked and shown in grey. v_{LSR}(MM1) = 35.2±0.4 km s^{-1} (from compact molecular line emission observed with the SMA; Cyganowski et al. (2011a,2022) estimate v_{LSR}(MM2)~37 km s^{-1} based on the velocity of the peak CH_3OH emission from the filament at the protobinary position. The ALMA images shown here have not been corrected for the primary beam response; all measurements were made from corrected images and corrected images are shown in Fig. 3. In (b) and (c), the 0.82-mm continuum contour levels are $\sigma_{npb} = 0.48$ mJy beam$^{-1}\times$ [-2, 4, 16, 40, 160, 280], where $\sigma_{npb} = 0.48$ mJy beam^{-1} is the rms of the 0.82-mm continuum image before primary beam correction. In all panels, the edge of the colour scale corresponds to the 20 per cent response level of the ALMA primary beam.

$1\sigma = 5.9$ mJy beam^{-1}. To maximize sensitivity, the H_2D^+ line data were imaged with multiscale clean, Briggs weighting with a robust parameter $R = 2$, and a velocity resolution $\Delta v = 0.4$ km s^{-1}. The resulting $H_2D^+(1_{1,0}–1_{1,1})$ image cube has a synthesized beam size of 0.762×0.551 arcsec^2 (PA = $-75°$) and an rms noise level of $1\sigma = 2.7$ mJy beam^{-1}. All measurements were made from images corrected for the primary beam response.

3 RESULTS

3.1 ALMA 0.82-mm continuum emission

The ALMA 0.82-mm continuum image is shown in Fig. 2 [in colour scale in (a) and as contours in (b) and (c)]. As expected, the 0.82-mm continuum emission displays a broadly similar morphology to the ALMA 1.05-mm continuum emission observed with similar angular resolution and sensitivity by Cyganowski et al. (2017) (1.05 mm $\theta_{syn} = 0.49 \times 0.34$ arcsec^2, $\sigma = 0.35$ mJy beam^{-1}). In the 0.82-mm continuum image, MM2 is located on a filamentary structure that extends to the north and southeast of MM2; this structure

encompasses the MM8, MM10, and MM16 cores identified by Cyganowski et al. (2017). To the southeast, the extended 0.82 mm continuum emission 'bridges' MM2 and the proto-O star MM1 (Ilee et al. 2016, 2018). To the east of MM2, $\sim 5\sigma$ extended emission also connects the dust continuum sources MM3 and MM5 (Cyganowski et al. 2017, see Fig. 1) to the main north–southeast dust filament, with the extended emission joining the main filamentary structure to the northeast of MM2. The MM7/MM9/MM13/MM17 group of mm sources (Cyganowski et al. 2017, Fig. 1), located north of MM2, is also detected in 0.82-mm continuum emission (see Fig. 2).

At the $\sim 0\farcs5$-resolution of our 0.82-mm image, MM2 appears as a strong, compact source of submillimetre continuum emission within the larger filamentary structure. To estimate the 0.82-mm properties of MM2, we fit a one-component two-dimensional Gaussian model to its 0.82-mm continuum emission using the CASA task imfit. From this one-component Gaussian fit, the fitted peak intensity of MM2 is $I_{peak} = 158.3±0.6$ mJy beam^{-1} and its fitted integrated flux density is $S_{0.82mm} = 390±2$ mJy. The fitted position of MM2 is $18^h13^m57\fs86094±0\fs00009$, $-18°54'14\farcs023±0\farcs001$ (J2000) and its deconvolved size is 614($±5$) mas × 584($±4$) mas (PA = $87° ± 8°$),

equivalent to $\sim 2070 \times 1970$ au^2 at $D = 3.37$ kpc. Notably, the single-component fit underestimates the peak intensity of MM2's 0.82-mm continuum emission: The residual image has an ~ 27 mJy beam^{-1} peak, which is $<0''.02$ from the fitted centroid position, surrounded by a negative ring. This indicates that a single-component Gaussian does not fully represent the emission, and points to the presence of additional substructure(s). This is consistent with the results from higher resolution ALMA observations, where MM2 is resolved to be a protobinary system with a projected separation of ~ 500 au (Cyganowski et al. 2022, see also Section 1). To check the robustness of the integrated flux density measurement from the Gaussian fit, we also use the CASA task imstat to measure the integrated flux density within the 30σ contour around MM2 and within a 2.0×1.0 arcsec^2 ellipse centred on its fitted position. These methods yield integrated flux density estimates of 401 ± 40 mJy and 327 ± 33 mJy, respectively,[3] within <3–16 per cent of the value from the Gaussian fit. This comparison suggests that the single-component Gaussian fit provides a reasonably robust estimate for the 0.82-mm integrated flux density of MM2, though we note that all estimates potentially include a contribution from the background filament emission (see also Section 6.2).

3.2 Molecular lines

3.2.1 H_2D^+ ($1_{1,0}$-$1_{1,1}$)

H_2D^+ ($1_{1,0}$-$1_{1,1}$) is undetected towards MM2 in our observations, to a 4σ limit of 10.8 mJy beam^{-1} (equivalent to a 4σ brightness temperature limit of 0.23 K). The non-detection of H_2D^+ towards MM2 is unsurprising, since MM2 is now known to host a protobinary system with two internally heated protostars (Cyganowski et al. 2022, see Section 1). H_2D^+ is destroyed by gas-phase reactions with CO, which evaporates from grains at temperatures >20 K; thus, H_2D^+($1_{1,0}$-1_1, 1) emission is only expected in the pre-stellar phase (e.g. Redaelli et al. 2021). Indeed, the few reported interferometric (ALMA) detections of H_2D^+($1_{1,0}$-1_1, 1) in high-mass star-forming regions in the literature are towards very quiescent, MIR-dark clumps and regions of IRDCs (e.g. Redaelli et al. 2021; Kong et al. 2023). In the more evolved cluster environment of G11.92$-$0.61, where there are many protostars heating the gas (including the MIR-bright massive protostars MM1 and MM3), H_2D^+ emission would only have been expected towards the cold, dense interior of a massive starless core.

3.2.2 N_2H^+ (4-3)

As shown in Fig. 2, extensive N_2H^+ (4-3) emission is detected around MM2 in our ALMA observations. Notably, the morphology of the integrated N_2H^+ (4-3) emission differs markedly from that of the 0.82-mm continuum (see Fig. 2a), with the peaks of the integrated N_2H^+ emission clearly offset from the continuum peak of MM2. The integrated N_2H^+(4-3) emission surrounding MM2 peaks to its northwest and southwest, at offsets of ~ 0.9 arcsec (~ 3000 au) and ~ 1.2 arcsec (~ 4000 au) from the continuum peak, respectively. Other than the peaks near MM2, the most significant feature in the N_2H^+ (4-3) integrated intensity map is a bow-like structure located towards the redshifted lobe of the high-velocity bipolar molecular

outflow driven by MM1 (Fig. 1, see also Cyganowski et al. 2011a, 2017). This intriguing feature, which may be associated with bow shocks caused by protostellar feedback from the proto-O star MM1, will be discussed in detail in a separate publication. The bow-like feature is also visible in the N_2H^+(4-3) peak intensity map in Fig. 2(b), which shows that the strongest N_2H^+ emission [543 mJy beam^{-1}, signal-to-noise ratio (SNR) ~ 92] is detected towards the filamentary structure to the southeast of MM2.

The intensity-weighted velocity (moment 1) map of the N_2H^+ (4-3) emission is shown in Fig. 2(c); however, examination of the data cube indicates that the spectra are, in general, too complex for the gas kinematics to be captured by a moment analysis. This complexity is illustrated by the sample spectra presented in Fig. 3. As shown by panels (a)–(c), the line profiles of the N_2H^+ (4-3) emission display significant spatial variation across the mapped region. In addition to negative bowls associated with missing short-spacing information (panel D, see also Section 2), N_2H^+ (4-3) absorption is detected against the submillimetre continuum towards MM2 (Fig. 3, panel B). As noted above and shown in Fig. 3, the N_2H^+ spectra are in general complex, with multiple emission peaks and/or absorption features. N_2H^+ (4-3) has 38 hyperfine structures (hfs) components spaced over $\lesssim 4.3$ km s^{-1} (Pagani, Daniel & Dubernet 2009). To assess the potential contribution of the hfs to the observed line profiles, we calculate the relative line strengths of the hfs components using the methods described in Daniel, Cernicharo & Dubernet (2006), and plot them in Panel (d) of Fig. 3. The strongest hfs components (with relative line strengths >0.1) are tightly grouped within $\lesssim 0.2$ km s^{-1} (i.e. within one channel in our image cube, which has $\Delta v = 0.2$ km s^{-1}; Section 2). We therefore argue that while the hfs will have some effect on the line profiles (as discussed further in Section 7.3), the multiple emission peaks observed in the spectra are predominantly caused by multiple velocity components present along the line of sight in the N_2H^+-emitting gas surrounding MM2.

We note that these observations are, to our knowledge, the first reported interferometric detection of N_2H^+ (4-3) in a high-mass star-forming region. N_2H^+ (4-3) has been detected with ALMA in a protoplanetary disc (where this transition was used to trace the CO snowline; Qi et al. 2013) and towards low-mass cores in Ophiuchus (Friesen et al. 2014). Interferometric observations of this transition are, however, relatively uncommon, as it is more challenging to observe than lower frequency N_2H^+ transitions (see also Section 7.3), which likely accounts for the lack of previous detections in high-mass star-forming regions. With single-dish telescopes, N_2H^+ (4-3) has been detected towards many low- and high-mass star-forming regions, with beams corresponding to physical resolutions of ~ 2000–86 000 au (e.g. van Dishoeck et al. 1992; Blake et al. 1995; Stark, van der Tak & van Dishoeck 1999; Friesen et al. 2010; Pillai et al. 2012; Ma et al. 2013; Kong et al. 2016; Koumpia et al. 2020; Miettinen 2020). For N_2H^+ (4-3) detections in nearby regions, the physical scale of the JCMT beam is similar to that of the synthesized beam of our ALMA data. The observations of Ophiuchus B2, L1544 and L1521f by Friesen et al. (2010) and Koumpia et al. (2020), for example, have a resolution of ~ 2000 au and 1σ rms noise of ~ 0.03–0.06 K (compared to $\sigma_{T_b} \sim 0.19$ K for our data). Interestingly, in these observations, while N_2H^+ is generally detected towards regions with submillimetre continuum emission, the strongest N_2H^+ (4-3) emission is found offset from the submillimetre continuum peaks (Friesen et al. 2010; Koumpia et al. 2020), as we observe in G11.92$-$0.61. Friesen et al. (2014) also report an offset between the N_2H^+ (4-3) and submillimetre continuum peaks in their ALMA study of low-mass cores in Ophiuchus, though these observations probe much smaller spatial scales (<200 au) and the authors note

---

[3]Uncertainties are estimated using equation (1) of Thwala et al. (2019), assuming 10 per cent absolute flux calibration uncertainty for ALMA in Band 7 (Cortes et al. 2023).
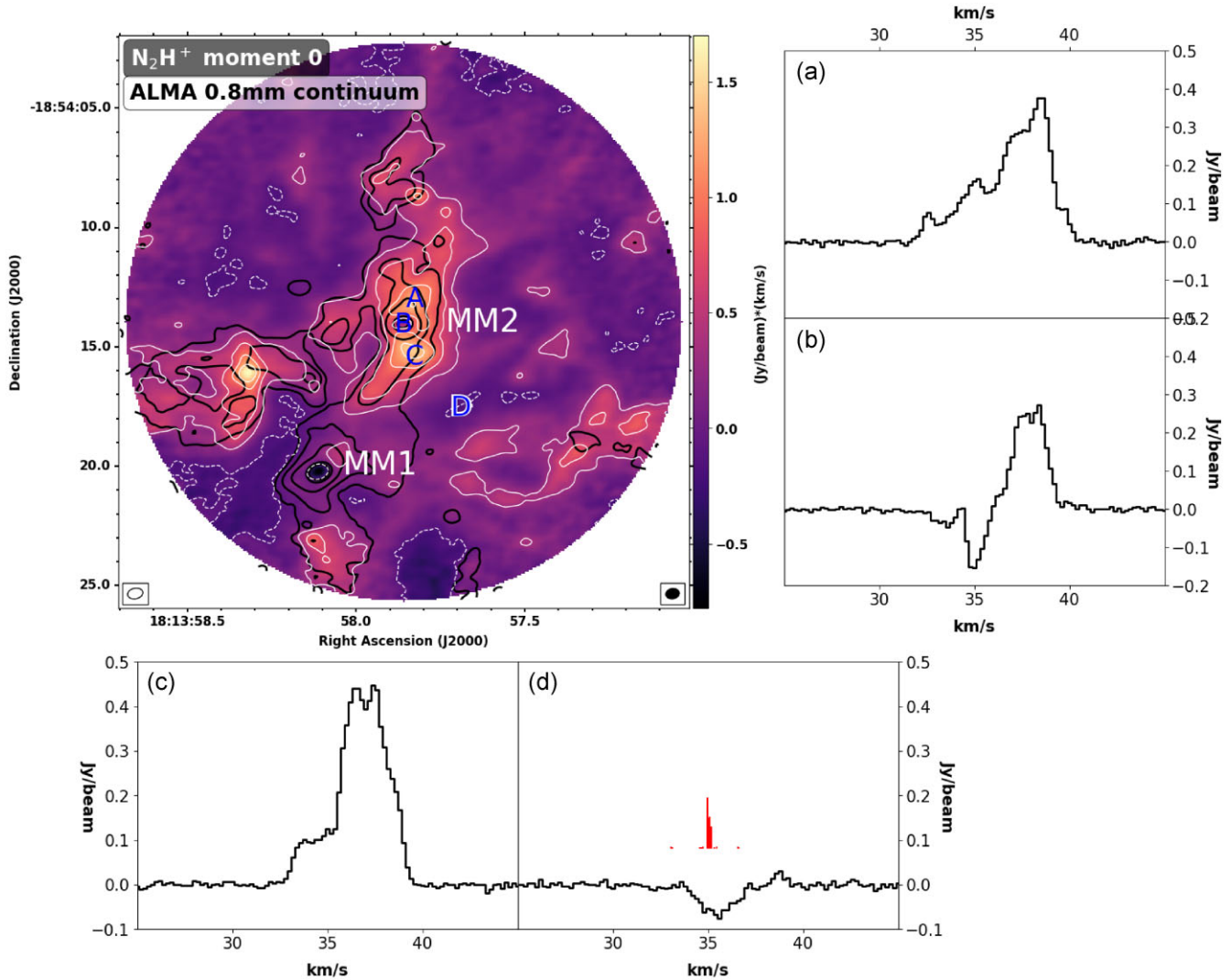
Figure 3. Top left panel: ALMA N_2H^+ (4-3) integrated intensity map (integrated over v = 27.0–42.0 km s^{-1}, colourscale and white contours, levels 0.066 Jy km s^{-1} × [−2, 5, 10, 15, 20], negative contours shown as dashed lines) overlaid with contours of the ALMA 0.82-mm continuum emission (black, levels: 0.5 mJy beam^{-1} × [5, 15, 40, 160, 280]), both corrected for the primary beam response. The edge of the colour scale corresponds to the 20 per cent response level of the ALMA primary beam and the synthesized beams of the N_2H^+ cube and the 0.82 mm continuum image are shown at bottom left (unfilled ellipse) and right (filled black ellipse), respectively. Panels labelled with letters show the N_2H^+ spectra extracted from the primary-beam-corrected image cube at the corresponding labelled locations on the integrated intensity map. Location A is the local peak of the integrated N_2H^+ emission to the north of MM2, B is the 0.82-mm continuum peak of MM2, C is the local peak of the integrated N_2H^+ emission to the south of MM2, and D is a representative negative bowl. The red vertical lines overlaid in panel (d) indicate the relative line strengths of the 38 hyperfine components of the N_2H^+ (4-3) transition (see Section 3.2.2) for $v_{lsr} = 35.0$ km s^{-1}.

that the observations are significantly affected by self-absorption and missing short-spacing data.

4 GAUSSIAN DECOMPOSITION ON THE N_2H^+ (4-3) CUBE

4.1 Gaussian decomposition with SCOUSEPY

To study the gas kinematics in the vicinity of MM2, we first apply Gaussian Decomposition to the N_2H^+ (4-3) cube using the SCOUSEPY package (Henshaw et al. 2016, 2019). SCOUSEPY is a Python implementation of the Semi-Automated multi-COmponent Universal Spectral-line fitting Engine (SCOUSE), designed to apply Gaussian Decomposition to large volumes of complex spectra in a semi-automated way. The SCOUSEPY version used in this work can

be downloaded from github.[4] The workflow consists of four stages, as outlined as follows:

In stage (1), SCOUSEPY generates spectral averaging areas (SAAs) and the spectra of SAAs based on spectral complexity. A 5σ mask (∼ 54 mJy beam^{-1}) was first applied to remove emission-free regions from the analyses that follow. As this data set exhibits strong spatial variation, we chose a conservative SAA size of 20 pixels (∼5300 au) with a filling factor of 0.6.[5] The velocity range and pixel range are set to include the whole data cube. Other parameters are kept at their default values. With these parameters applied to the N_2H^+ data cube,

---

[4]https://github.com/jdhenshaw/scousepy/tree/delta

[5]This filling factor selects SAAs with significant emission in more than 60 per cent of the enclosed pixels; see SCOUSEPY documentation (linked from github) and Henshaw et al. (2016) for additional details.

SCOUSEPY generates 452 SAAs along with their spectra; as they are Nyquist sampled, each SAA overlaps with neighbouring SAAs. In the area covered by SAAs, the program identifies a total of 48 141 individual spectra (corresponding to individual pixels in the data cube) to be analysed.

In stage (2), SCOUSEPY applies Gaussian Decomposition to the 452 spectra of SAAs generated in stage 1). The SCOUSEPY version used in this work has introduced derivative spectroscopy (Lindner et al. 2015; Riener et al. 2019) to assist with multicomponent Gaussian fitting. The program will first filter spectra with Gaussian kernels and then calculate derivatives of the smoothed spectra up to the fourth order. The derivative spectroscopy technique measures the locations of spectral components by searching for 'bumps', which mathematically means the local minimum of negative curvature in the filtered spectra (i.e. second derivative < 0, third derivative $= 0$, and fourth derivative > 0, see details in Lindner et al. 2015). SCOUSEPY first fits the spectra with initial guesses adopted from the measurements of derivative spectroscopy. The fitting is controlled by two input parameters: the SNR and the standard deviation of the Gaussian kernel (σ_{ker}) used for filtering. We vary the SNR from 3 to 5 and the σ_{ker} from 1 to 3 channels to obtain satisfying fits for $\gtrsim$ 96 per cent of the SAA spectra; for an additional four SAA spectra, increasing the SNR to 7–9 yields reasonable fits. For the remaining SAA spectra, we use the manual fitting option of SCOUSEPY to fit the spectra 'by hand' to obtain physically reasonable fits. In some cases, for example, derivative spectroscopy fits artificially broad redshifted components; we manually fit multiple weak components to the red tails of these spectra to obtain physically reasonable fits. There is only one spectrum (out of the 452 SAA spectra) which cannot be fitted well either by the derivative spectroscopy fitting or manual fitting. We flag the corresponding SAA at the end of stage (2) so that the problematic fit is not used to provide initial guesses for fits to individual spectra. The problematic SAA overlaps with neighbouring SAAs, so SCOUSEPY fits the spectra of the pixels within the flagged SAA based on the fits for the surrounding SAAs.

Stage (3) uses the fits for the spectra of SAAs as initial guesses to conduct Gaussian decomposition for the 48 141 individual spectra. SCOUSEPY adopts the fits from stage (2) as initial guesses and applies automated Gaussian decomposition to the individual spectra within each SAA. To control the process of automated Gaussian decomposition, users set tolerance levels using six parameters: T_0, T_1, T_2, T_3, T_4, and T_5. T_0 is newly introduced to the SCOUSEPY version used here. It limits the maximum difference between the number of fitted components for spatially averaged spectra and individual spectra. T_1 sets the threshold for amplitude, below which weak components are discarded before subsequent analyses. T_2 and T_3 control the full width at half-maximum (FWHM) of fitted components; T_4 limits the centroid velocity. T_5 sets the minimum separation in centroid velocity between two adjacent Gaussian components. Detailed descriptions of these parameters can be found in Henshaw et al. (2016).

In the final stage, SCOUSEPY selects the best-fitting models with Akaike information criterion (AIC) for the 48 141 individual spectra. As SAAs are Nyquist sampled, each of the individual spectra may hold multiple solutions of Gaussian decomposition. The program identifies locations with multiple models and chooses the models with the lowest AIC values as the best-fitting ones.

We first run SCOUSEPY with default tolerance levels in stage 3: we refer to these results as 'version 0'. This version generates reasonable fits for ~ 80 per cent of the spectra. However, given the complicated spectral structure and significant spatial variation of this data set, the automated fitting could miss or overfit components at certain regions. For example, in version 0 SCOUSEPY identifies two adjacent peaks

Table 2. Summary of tolerance levels used in stage 3 of the Gaussian decomposition using SCOUSEPY.

Parameter	Version 0	Version 1	Version 2
T_0	2.0	2.0	2.0
T_1	3.0	3.0	3.0
T_2	1.0	1.0	1.0
T_3	2.5	4.0	2.5
T_4	2.5	2.5	1.0
T_5	0.5	0.5	0.5

as a single velocity component a few pixels to the north of MM2. Therefore, a single set of tolerance levels may not be ideal for the whole data set. To test the performance of automated fitting, we run stage (3) with another two sets of tolerance levels labelled as version 1 and version 2. In version 1, we relax the T_3 constraint on the maximum velocity dispersion of fitted components by 60 per cent compared with version 0; in version 2, we tighten the T_4 constraint on the fitted centroid velocity to 40 per cent of the value in version 0 (see Table 2). We compile all the results from the three versions and select the models with the lowest AIC values as the best-fitting ones. More than 79 per cent of the final best-fitting models are adopted from version 0; while 8 per cent are taken from version 1 and 3 per cent from version 2. For ~ 9.7 per cent of the pixels within the mask applied in stage 1, SCOUSEPY could not find best-fitting models which satisfy all the conditions mentioned above. The tolerance levels applied in each version are summarized in Table 2. The contribution of each version to the final results is shown in the left panel of Fig. 4. Examples of the SCOUSEPY fits to the N_2H^+ spectra are shown in Fig. A1.

We note that SCOUSEPY is not designed to reproduce absorption and that Gaussian decomposition is applied only to the N_2H^+ emission. The analyses described below also focus only on the N_2H^+ emission features.

4.2 Results and basic statistics

We obtain best-fitting models for 43 079 spectra, and a total of 96 157 Gaussian velocity components. This corresponds to an average of ~ 2.2 components per pixel. Indeed, more than 66 per cent of the spectra are fitted with models containing multiple velocity components. The right panel of Fig. 4 shows the distribution of the number of velocity components at each pixel. Pixels with zero components do not have accepted models (see Section 4.1). SCOUSEPY fits from 1 to 6 components to individual spectra (with no maximum number of components imposed), with a median number of components of 2. As illustrated by the right-hand panel of Fig. 4, the complexity of the velocity structure varies spatially. The vicinity of MM2 is among the regions with the most complex spectra: to the north of MM2, the median number of components/pixel reaches 4, and to the south of MM2 the median number of components/pixel is 3.

The top panel of Fig. 5 presents a histogram of the centroid velocities of the best-fitting components. The centroid velocities range from 27.6 to 42.1 km s^{-1}, with a mean of 35.7 km s^{-1}, a standard deviation of 1.8 km s^{-1}, and an interquartile range of 2.7 km s^{-1}. The velocity histogram deviates from a Gaussian-like distribution in having two main groups of peaks, at ~ 34.5 and ~ 37 km s^{-1}, possibly indicative of large-scale velocity gradients across the region. Sharp spikes and shoulders are also visible, reflecting complex velocity substructures on small spatial scales. The bottom panel of Fig. 5 plots amplitude against centroid velocity
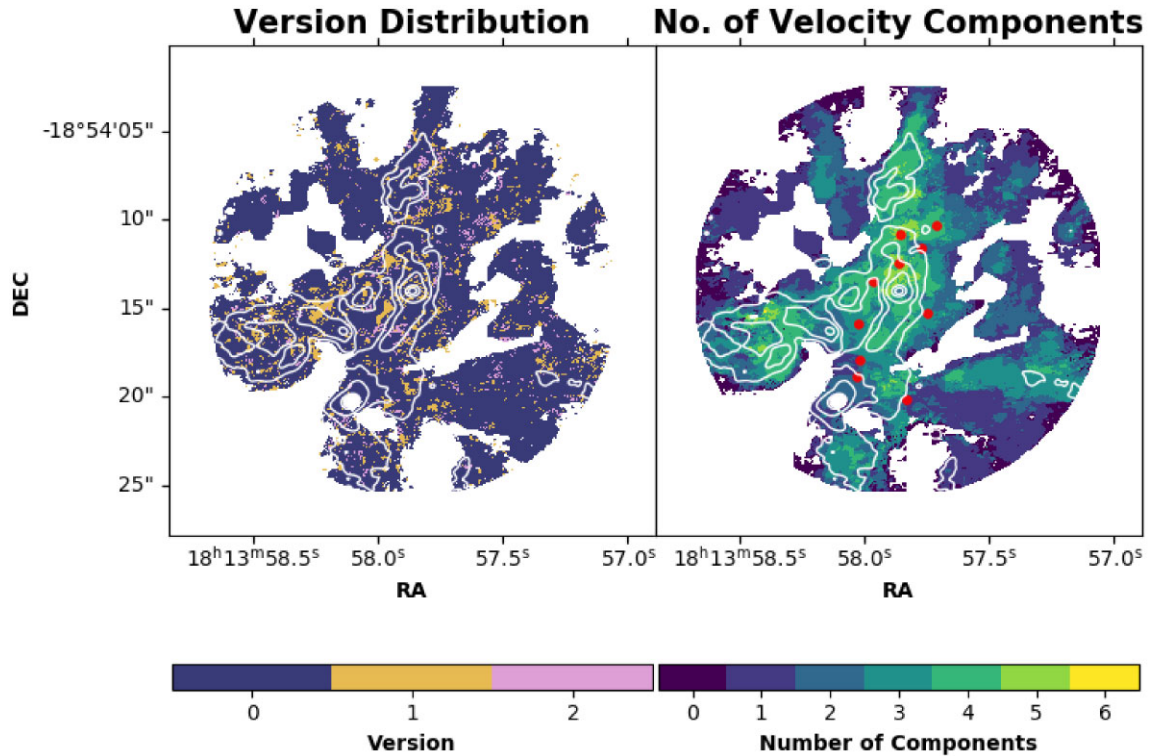
Figure 4. Left panel: the version of the best-fitting model employed in the final compiled solution for each of the 48 141 individual spectra. The numbers on the colour bar correspond to the versions described in Section 4.1. Right panel: distribution of the number of velocity components in the best-fitting models. Red circles mark the locations of the 10 spectra selected for hyperfine structure fitting (see Section 7.3). ALMA 0.82-mm continuum contours (white, levels: 0.5 mJy beam^{-1} × [5, 15, 40, 160, 280]) are overlaid in both panels.
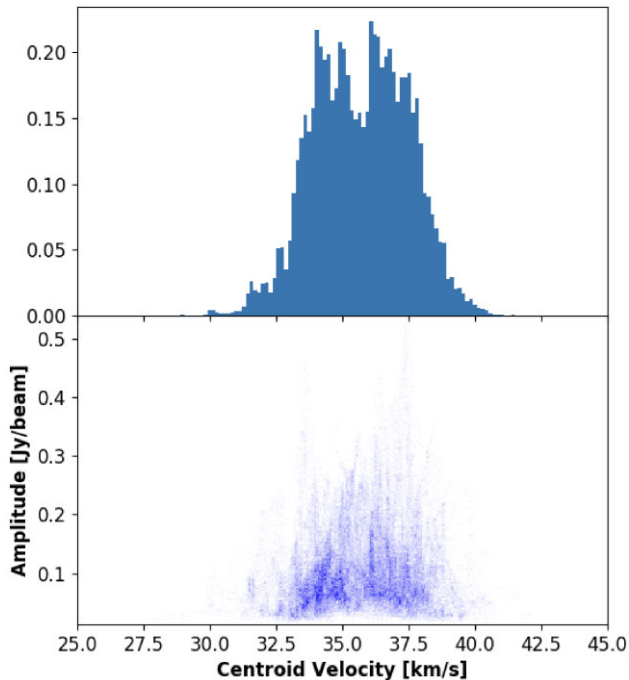

Figure 5. Top panel: histogram of centroid velocities for the best-fitting components (bin size: 0.25 km s^{-1}). Bottom panel: fitted amplitudes of velocity components versus centroid velocity.
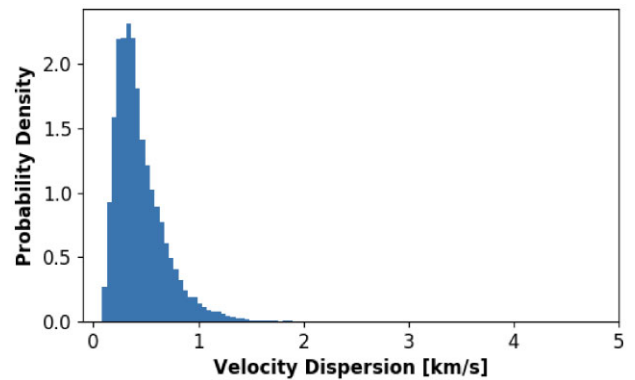
Figure 6. Histogram of velocity dispersion for the best-fitting components (bin size: 0.06 km s^{-1}).

for all fitted components. The fitted amplitudes range from ∼12.5 to ∼539.4 mJy beam^{-1}, with a median of ∼ 93.3 mJy beam^{-1}. The strongest components generally fall within the interquartile range in velocity, while the components on the tails of velocity distribution are generally weaker.

The fitted velocity dispersion ranges from 0.1 to 4.6 km s^{-1}, with a median of 0.4 km s^{-1} and an interquartile range of 0.3 km s^{-1}. As shown in Fig. 6, the histogram of σ_v is highly asymmetric, with a tail extending to 12× the median value. This asymmetry is also reflected in a positive skewness of ∼ 2.6. We therefore present median and interquartile values instead of mean and standard deviation
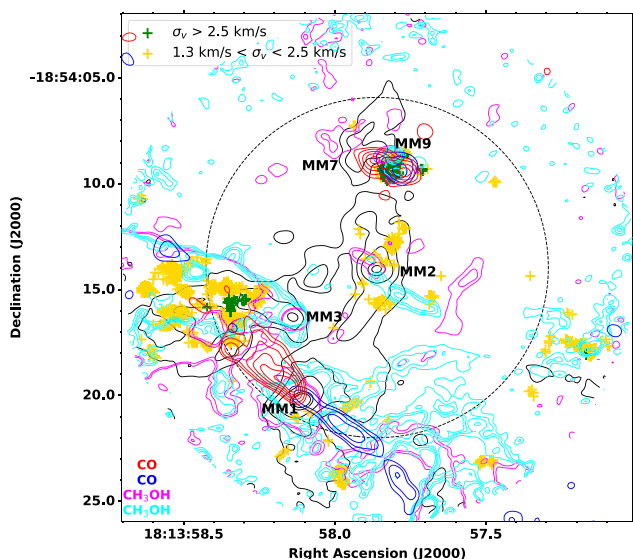
Figure 7. Spatial distribution of fitted velocity components with high-velocity dispersions: yellow crosses mark $1.3 < \sigma_v < 2.5 \, \text{km s}^{-1}$ and green crosses mark $\sigma_v > 2.5 \, \text{km s}^{-1}$, where 1.3 and 2.5 km s^{-1} are the 99th and 99.9th percentile of the velocity dispersion distribution. Contours show the ALMA 0.82 mm continuum (black, levels: 0.5mJy beam^{-1} × [5, 15, 40, 160, 280]), SMA blueshifted and redshifted ^{12}CO (3-2) line emission from Cyganowski et al. (2014, 2017) (blue: [4, 6, 9] × 1.0 Jy km s^{-1}, red: [4, 6, 9, 12, 15, 18] × 1.0 Jy km s^{-1}), and ALMA blueshifted and redshifted CH$_3$OH ($4_{-1,3}-3_{0,3}$) line emission from Cyganowski et al. (2022) (cyan: [4, 7, 10, 15] $\times \sigma$ = 5.5 mJy km s^{-1}, magenta: [4, 7] $\times \sigma$ = 3.3 mJy km s^{-1}). Contours are from images corrected for the primary beam response. The dashed black circle shows the FWHP (50 per cent response) level of the ALMA primary beam, and the ALMA images are masked at its 20 per cent response level.

values to better describe the concentration and dispersion of σ_v. Investigating the spatial distribution of the high-velocity-dispersion tail, we find that the highest-dispersion components (99.9th percentile, $\sigma_v > 2.5 \, \text{km s}^{-1}$), shown as green crosses in Fig. 7, are associated with the protostellar outflows from MM7/9 and from MM1 and/or MM3 (Cyganowski et al. 2011a, 2014, 2017). As shown in Fig. 7, many components with $1.3 < \sigma_v < 2.5 \, \text{km s}^{-1}$ (99th to 99.9th percentile, shown as yellow crosses) are also spatially associated with the outflows from MM1/3/7/9 or with MM2's outflow, though some broad components are also distributed along the north–southeast filamentary structure near MM2. (We focus here on high-dispersion points within the FWHP extent of the ALMA primary beam, where the data are most sensitive, see Fig. 7.) The spatial correlation between many high-velocity-dispersion components and known protostellar outflows indicates that we are observing the imprint of protostellar feedback on the dense molecular gas, which will be discussed in detail, in conjunction with the bow-like feature mentioned in Section 3.2.2, in a separate publication.

5 HIERARCHICAL CLUSTERING OF VELOCITY COMPONENTS

5.1 Hierarchical clustering with ACORNS

To further analyse the velocity structure within the N$_2$H$^+$-emitting gas, we conduct hierarchical clustering of the velocity components

extracted in Section 4 using ACORNS[6] (Agglomerative Clustering for Organising Nested Structures, Henshaw et al. 2019). ACORNS is designed to characterize the hierarchical structure within discrete spectroscopic data (e.g. data points in position–position–velocity space) based on the hierarchical agglomerative clustering technique. A comprehensive description of the philosophy and parameters of this package can be found in Henshaw et al. (2019, appendix B).

Before running the ACORNS clustering, we perform a cleaning of the velocity components extracted by SCOUSEPY. We discard all pixels without fits (~ 5 per cent of the total SCOUSEPY data), remove components with peak intensities $< 3\sigma$ (where σ is the rms, measured individually for each spectrum), and remove components where either the peak intensity or the velocity dispersion is smaller than its associated uncertainty. We then conduct the ACORNS clustering only on the remaining velocity components, which represent $\sim$94 per cent of the total number of extracted components.

We first perform ACORNS clustering of the SCOUSEPY fits in position–position–velocity space, with parameters based on the spatial and spectral resolution of our N$_2$H$^+$ data. The minimum radius of a cluster is set to 4× the pixel size to ensure that the minimum number of data points in a cluster is comparable to the number of pixels in a synthesized beam ($\sim$52). The minimum height above the merge level is set to be 3× the mean rms and the maximum absolute velocity difference between two components identified as linked is set to 0.2 km s^{-1}, the channel width of the N$_2$H$^+$ image cube (Section 2). We add an additional clustering criterion based on the velocity dispersion, requiring the absolute difference in velocity dispersion between two linked components to be smaller than 0.2 km s^{-1}. With these parameters, ACORNS identifies a total of 198 clusters, which contain $\sim$ 95 per cent of the input velocity components.

To investigate the sensitivity of the ACORNS results to the choice of input parameters, we performed additional clustering runs varying the peak intensity cutoff and the relaxation of linking lengths. In these tests, we found that applying a 5σ (rather than 3σ) threshold to the velocity components excluded a significant amount of data ($\sim$23 per cent) and so did not reflect the extended structure of clusters. We then tested the clustering criteria for position, velocity, and velocity dispersion with different relaxation levels of linking lengths, relaxing the linking criteria by 20 and 50 per cent to enable clusters to grow. These tests showed that the clustering results are relatively robust against relaxation: the percentage of data points assigned to clusters grew by only $\sim$0.3 and $\sim$0.8 per cent in the 20 and 50 per cent relaxed versions, respectively, indicating that the vast majority of pixels are clustered without the need for relaxing the criteria. Based on these results, we adopt the original clustering run described above, with a 3σ cutoff and without relaxing the linking criteria, for the remainder of our analysis.

5.2 Results and statistics

Fig. 8 shows the hierarchical system (referred to as a 'forest') identified by the ACORNS PPV clustering. In general, a dendrogram 'forest' consists of a number of 'trees'; each tree may have substructure(s), which are referred to as 'branches' if they have further substructure(s), or 'leaves' if they do not (see e.g Rosolowsky et al. 2008; Goodman et al. 2009). Trees with no substructure are also categorized as leaves. Our ACORNS PPV clustering identifies a total of

---

[6] ACORNS is a publicly available PYTHON package, and can be downloaded from https://github.com/jdhenshaw/acorns.
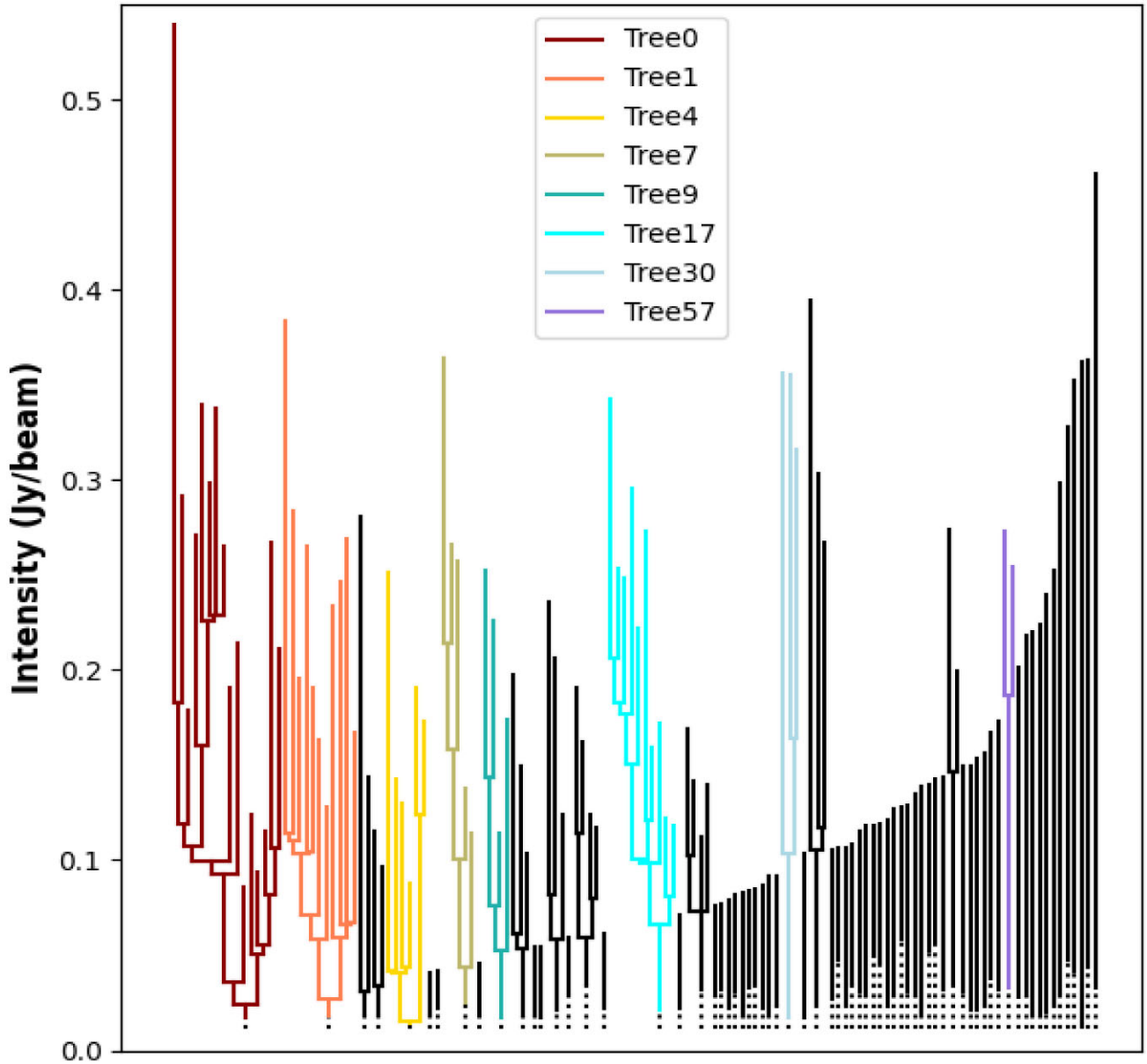
Figure 8. Dendrogram of the hierarchical system in the N_2H^+ (4-3)-emitting gas identified by ACORNS, referred to a 'forest'. The forest consists of 70 trees, which are position- and velocity-coherent clusters. ~ 23 per cent (16/70) of the trees have branches or leaves (i.e. substructure). The eight most dominant trees (Section 5.2) are plotted in colour. Substructure is indicated by short horizontal lines and the highest points of the leaves represent their peak intensities.

70 trees, of which 16 (~ 23 per cent) have substructure, i.e. branches or leaves. Eight of the identified trees together comprise $\gtrsim 60$ per cent of the data points used for the clustering analysis. These trees, shown in colour in Fig. 8, are designated Tree 0, Tree 17, Tree 1, Tree 4, Tree 9, Tree 7, Tree 30, and Tree 57 (listed in order of decreasing number of assigned data points). In this paper, we focus our analysis on Tree 0, the dominant feature of the hierarchical system. Tree 9 will also be discussed in Section 6.3 as supporting evidence for the physical scenario proposed in this work. Analysis of other trees and their substructures will be presented in separate publications focusing on different scientific topics.

Tree 0 contains ≈ 20 per cent of the total velocity components, the most of any tree, and the components with the highest peak intensity. Fig. 9 shows maps of the spatial distribution of the peak intensities, centroid velocities, and velocity dispersions of the

velocity components in Tree 0. The maximum peak intensity in Tree 0 is 539.4 mJy beam^{-1} and the median peak intensity is 122.7 mJy beam^{-1}. The centroid velocities of the components in Tree 0 span a relatively narrow range of 35.0–38.8 km s^{-1}, compared to the range of 27.6– 42.1 km s^{-1} for all fitted components (see Section 4.2). The median velocity of Tree 0, which is 37.0 km s^{-1}, falls within the higher velocity of the two main peaks seen in Fig. 5. The median velocity dispersion of Tree 0 agrees with that of the full data set (~ 0.4 km s^{-1}), but Tree 0 lacks the high-dispersion tail seen in Fig. 6, with a maximum velocity dispersion of 1.5 km s^{-1}. Spatially, Tree 0 appears to trace the major features in the moment 8 map (Fig. 2b), including the main north–southeast filamentary structure and the extended emission that lies to the west of the southern end of the main filament. The strongest emission in Tree 0 is located in the filamentary structure to the southeast of MM2 (see Fig. 9). Notably,
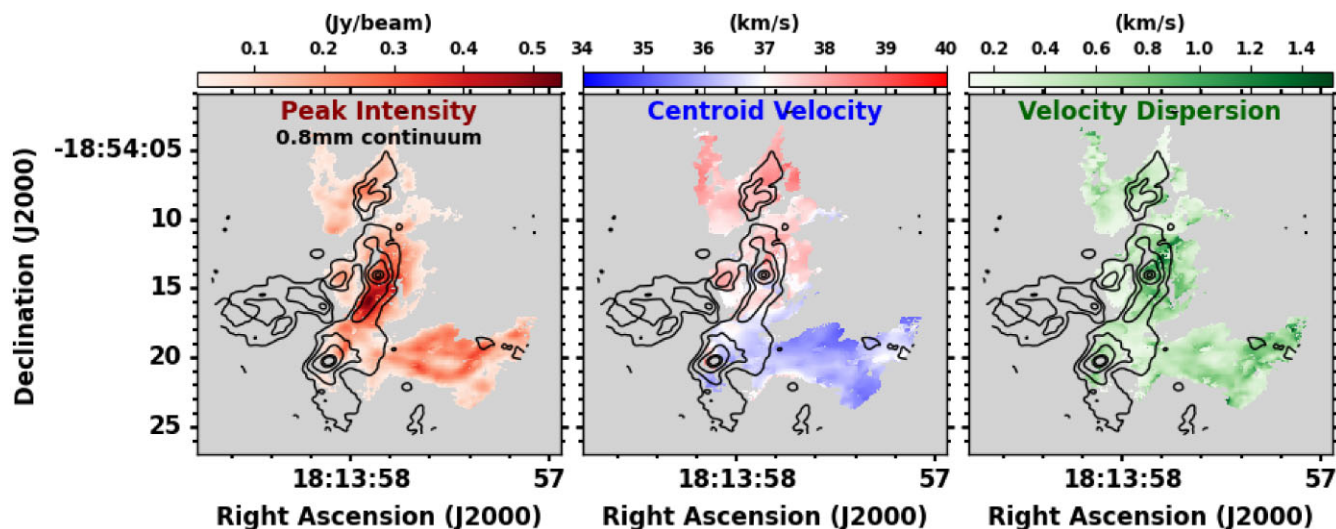
Figure 9. Left panel: distribution of peak intensities of the velocity components of Tree 0. Middle panel: centroid velocity map of Tree 0. Right panel: velocity dispersion map of Tree 0. ALMA 0.82-mm continuum contours (black, levels: 0.5mJy beam$^{-1} \times$ [5, 15, 40, 160, 280]) are overlaid in all panels.
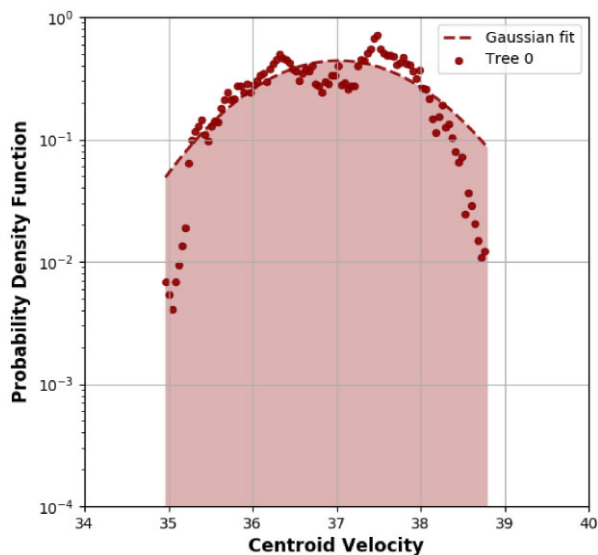
Figure 10. Probability distribution function (PDF) of the centroid velocities of the components in Tree 0 (filled circles), overlaid with the best-fitting Gaussian model to the velocity PDF (dashed line).

the centroid velocity map of Tree 0 (shown in the middle panel of Fig. 9) reveals a roughly north–south velocity gradient along the main filamentary structure, which we consider further in Section 6.1. The most notable feature of the velocity dispersion map (right panel of Fig. 9) is an area of enhanced velocity dispersion ($\sim$ 50–70 per cent) around MM2, within a radius of $\sim 3''$.

Fig. 10 shows the probability distribution function (PDF) of the centroid velocities of the components in Tree 0. As illustrated by Fig. 10, the velocity PDF is not well represented by a Gaussian model, with excesses at $\sim$36.3 and $\sim$37.8 km s^{-1}, and moderation in the tails. The kurtosis of the velocity PDF of Tree 0 is estimated to be 2.3; a value <3 (the kurtosis of the Gaussian distribution) implies lighter tails, consistent with the features of the PDF. While simulations of turbulence suggest Gaussian-like velocity PDFs (e.g. Federrath 2013), observations do not always agree (e.g. Federrath et al. 2016; Henshaw et al. 2019). In their study of the Galactic Centre molecular

cloud G0.253+0.016, Federrath et al. (2016) interpret double-peaked deviations from a Gaussian distribution as the result of a large-scale velocity gradient, and note that observational noise, the excitation of the molecular tracer, and smaller scale systematic motions may also contribute to deviations from a Gaussian model (see also Henshaw et al. 2019). We suggest that the double-peak feature in the Tree 0 velocity PDF may be caused by the large-scale velocity gradient seen in Fig. 9, similar to the case in Federrath et al. (2016).

6 FILAMENTARY ACCRETION FLOWS

6.1 Velocity gradient

As discussed in Section 5.2, the centroid velocity map of Tree 0 shows an $\sim$north–south velocity gradient, consistent with this tree's double-peaked velocity PDF. As shown in Fig. 9 (middle panel), this velocity gradient goes through MM2 and extends to MM1 to the south and to the MM7/MM9/MM13/MM17 group of sources to the north of MM2. To analyse the gas kinematics in the surroundings of MM2, we select a position- and velocity-coherent substructure (a 'branch') of Tree 0 that encompasses the immediate environment of MM2, designated Branch 8. The centroid velocity map of this branch is shown in Fig. 11. On the plane of the sky, Branch 8 is $\sim$0.17 pc long and $\sim$0.05 pc wide. It hosts the brightest velocity components of Tree 0 (with a peak intensity of 539.4 mJy beam^{-1}), and has a median intensity of 209.1 mJy beam^{-1}, which is higher than the median intensity of Tree 0 by a factor of $\sim$1.7. The centroid velocities in Branch 8 range from 35.9 to 38.6 km s^{-1} with a median value of 37.3 km s^{-1}, covering $\sim$ 71 per cent of the velocity range of Tree 0. Branch 8 also contains the broadest velocity components of Tree 0, with a maximum velocity dispersion of 1.5 km s^{-1} and a median of 0.5 km s^{-1}.

We measure the magnitude and direction of the velocity gradient of Branch 8 using the methods proposed by Goodman et al. (1993). A linear gradient of centroid velocities is described by the following equation:

$$v = v_0 + a\Delta\alpha + b\Delta\delta, \tag{1}$$

where $\Delta\alpha$ and $\Delta\delta$ are the variations in right ascension and declination in units of radians; a and b are the projections of the velocity gradient
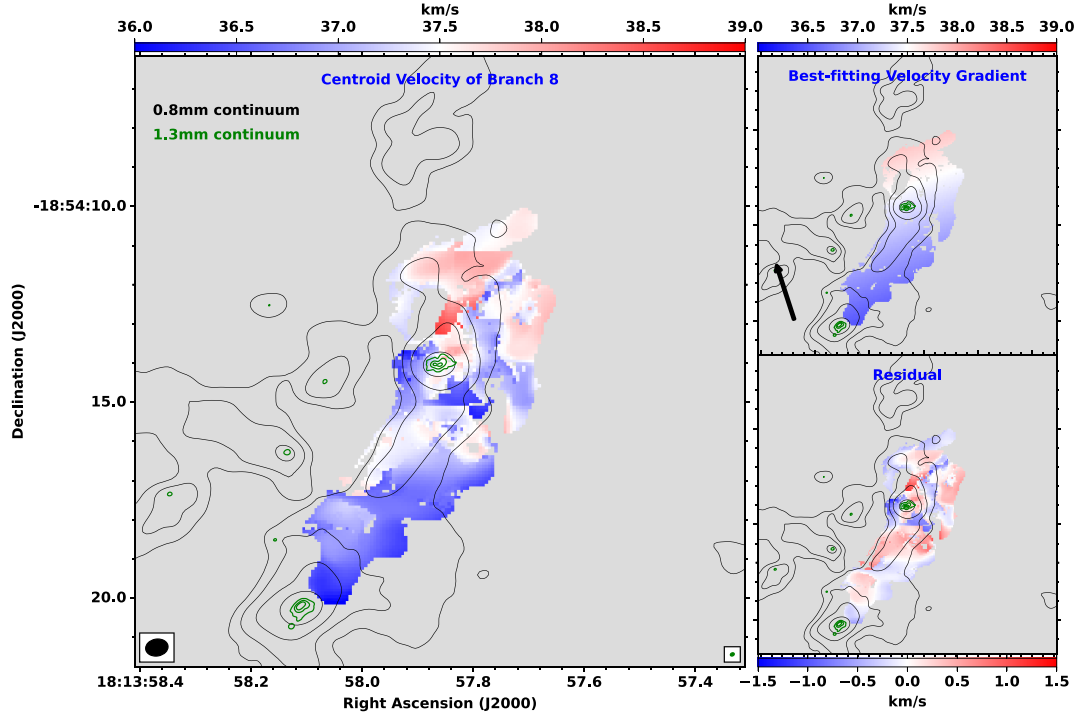
Figure 11. Left panel: centroid velocity map of Branch 8. Top right panel: map of best-fitting velocity gradient; its direction is indicated by the black arrow. Bottom right panel: residual map, generated by subtracting the best-fitting velocity gradient from the observations. In all panels, ALMA 0.8-mm continuum contours (black; contour levels: $0.5 \times [5, 15, 40, 160, 280]$ mJy beam^{-1}) and ALMA 1.3-mm continuum contours from Ilee et al. (2018) (green; contour levels: $0.06 \times [10, 50, 150]$ mJy beam^{-1}) are overlaid. The synthesized beams of the 0.8- and 1.3-mm data are shown in the left-hand panel, at bottom left and right, respectively.

per radian on the axes of right ascension and declination, respectively; and v_0 is the systemic velocity. The magnitude of the velocity gradient $|\nabla v|$ is given by

$$|\nabla v| = \frac{\sqrt{a^2 + b^2}}{D}, \qquad (2)$$

where D is the distance to the source (3.37 kpc, Section 1). The direction of increasing velocity (east of north) is

$$\Theta = \arctan\left(\frac{a}{b}\right). \qquad (3)$$

We estimate the values of a and b by fitting a first-degree bivariate polynomial to the centroid velocity map of Branch 8 using LMFIT.[7] The uncertainties associated with the centroid velocities from SCOUSEPY are included to constrain the fitting. We estimate the velocity gradient exhibited by Branch 8 to be 10.5 ± 0.2 km s^{-1} pc^{-1} in a direction of $\sim 18.9°$ (east of north) over a spatial scale of ~ 0.17 pc. The best-fitting model is shown in the top right panel of Fig. 11, with the black arrow indicating the direction of the fitted velocity gradient. The bottom right panel of Fig. 11 shows the residual map, calculated by subtracting the best-fitting model from the centroid velocity map. The residuals range from -1.3 to 1.2 km s^{-1}.

In other filamentary high-mass star-forming regions, the magnitudes of velocity gradients measured along (sub)filaments vary by an order of magnitude, with a trend of larger velocity gradients at smaller spatial scales: ~ 0.2–0.9 km s^{-1} pc^{-1} at >1–8 pc scales (e.g.

Bally et al. 1987; Peretto et al. 2014; Tackenberg et al. 2014; Zhang et al. 2015; Hacar et al. 2017; Yuan et al. 2018; Chen et al. 2019; Treviño-Morales et al. 2019; Hu et al. 2021; Beltrán et al. 2022), ~ 0.7–0.8 km s^{-1} pc^{-1} at ~ 1 pc scales (e.g. Fernández-López et al. 2014; Henshaw et al. 2014), and $\gtrsim 1$–20 km s^{-1} pc^{-1} at ~ 0.1–0.5 pc scales (Henshaw et al. 2013; Liu et al. 2016; Hacar et al. 2018; Williams et al. 2018; Li et al. 2022). This finding is reinforced by a recent systematic study of the gas kinematics of a large sample of filaments using ALMA H^{13}CO$^+$ data, where the magnitude of the velocity gradients increases from a few $\times \sim 1$ km s^{-1} pc^{-1} to a few $\times \sim 10$ km s^{-1} pc^{-1} as the extent over which the velocity gradients are measured decreases from ~ 1 to ~ 0.1 pc (Zhou et al. 2022).

Zhou et al. (2022) argue that the smaller velocity gradients at larger scales are likely caused by pressure-driven inertial inflows shaped by either turbulence or gravity at large spatial scales, while the larger velocity gradients at smaller scales are likely attributable to the gravity of dense structures (e.g. cores and/or the hubs of hub-filament systems). The latter scenario agrees well with our measurements for Branch 8 (~ 10.5 km s^{-1} pc^{-1} over ~ 0.17 pc). For comparison, we also estimate the velocity gradient of Tree 0 using the same technique, which gives 9.3 ± 0.1 km s^{-1} pc^{-1} in a direction of $\sim 34.7°$ (east of north) over ~ 0.47 pc. The magnitude of the velocity gradient increases moderately (1.2 km s^{-1} pc^{-1}, ~ 13 per cent) when the spatial scale decreases by 0.3 pc (~ 60 per cent). We note that the variation in observed velocity gradients along filaments may also be influenced by projection effects: The observed magnitude of the velocity gradient along a filament will be smaller if the orientation of the filament is closer to the plane of sky.

Simulations and observations suggest that gravity is dynamically more important at higher densities and smaller spatial scales (e.g.

---

[7]LMFIT is a PYTHON package designed for non-linear least-squares minimization and curve-fitting based on scipy.optimize. The package is publicly available via https://github.com/lmfit/lmfit-py.

Smilgys & Bonnell 2016; Chen et al. 2019). Williams et al. (2018) find that >60 per cent of the dense cores in the IRDC SDC13 are associated with the peaks of velocity gradients traced by NH_3, which is interpreted as a signature of cores accreting material from their parental filaments. We note that the southeast end of Branch 8 reaches the 160σ 0.8-mm continuum contour around the proto-O star MM1, roughly $\sim$1700 au from the centre of MM1. The gravity of MM1 (with an enclosed mass of $\sim$40 $M_\odot$, Ilee et al. 2018) is expected to dominate over pressure support in its local ($\lesssim$0.1–0.6 pc) environment (Williams et al. 2018; Chen et al. 2019). As a test of minimizing the effects of MM1, we measured the velocity gradient adopting the southern end of the 15σ contour extending from MM2 to MM1 as a boundary, and obtain a value of 8.4 ± 0.2 km s^{-1} pc^{-1} in the direction of $\sim$14° (east of north). This suggests that introducing an artificial boundary has a limited ($\sim$20 per cent) effect on the velocity gradient measurement. The GHC model (Vázquez-Semadeni et al. 2017, 2019) also suggests that global collapse driven by the large-scale gravitational potential well and local collapse driven by small-scale overdensities take place concurrently. In this scenario, the observed velocity gradient of Branch 8 would most likely be caused by a combination of large-scale gas flows towards the centre of the massive cluster and small-scale gas flows towards both MM1 and MM2 (as seen in Peretto et al. 2014). In this context, it would be difficult to define a physically meaningful boundary within a continuity of gas flows. We thus adopt the measurement using the full extent of Branch 8 in our analysis.

6.2 Mass inflow rate

Velocity gradients along filaments are commonly interpreted as signatures of longitudinal gas flows (e.g. Kirk et al. 2013; Peretto et al. 2014; Liu et al. 2016; Lu et al. 2018; Yuan et al. 2018; Chen et al. 2019, 2020b; Treviño-Morales et al. 2019; Hu et al. 2021). If the filamentary structure observed in G11.92−0.61 is oriented such that its southeast end is further from the observer than its north-west end, the observed velocity gradient in Branch 8 is consistent with accelerating accretion flows towards MM2.[8]

Based on the hypothesis of filamentary accretion flows, we can derive the mass inflow rate using the velocity gradient and mass of Branch 8 following the procedure in Kirk et al. (2013). We estimate the gas mass of Branch 8 from its 0.82-mm integrated flux density, which is measured by integrating the intensity within the boundary of Branch 8 using the CASA task imstat, under the simple assumptions of optically thin, isothermal dust emission as (see e.g Cyganowski

et al. 2011a, 2017)

$$M_{\rm gas}(M_\odot) = \frac{4.79 \times 10^{-14} R S_\nu(\mathrm{Jy}) D^2(\mathrm{kpc})}{B(\nu, T_{\rm dust})\kappa_\nu}, \qquad (4)$$

where R is the gas-to-dust mass ratio (assumed to be 100), S_ν is the integrated flux density, and D is the distance to G11.92−0.61. We adopt $\kappa_{0.82\,\rm mm} = 2.3$ cm^2 g^{-1}, based on linear interpolation of the Ossenkopf & Henning (1994) values for MRN grains with thick ice mantles and $n_{H_2} = 10^6$ cm^{-3} (column 7 of their table 1), and a dust temperature range $T_{\rm dust} =$15–25 K. Our adopted dust temperature range is informed by clump-scale NH_3 temperature measurements for G11.92−0.61 ($T_{\rm kin} \sim$26 K from single-component fitting and $T_{\rm kin} \sim$14 and 54 K from two-component fitting, where the 54 K-component is attributable to the immediate environment of MM1; Cyganowski et al. 2013) and by temperature maps derived from VLA NH_3 observations of other EGOs (e.g. Brogan et al. 2011, their Fig. 3). With our adopted parameters, we estimate the mass of Branch 8 as $\sim$30–65 $M_\odot$. For a simple cylindrical model with a length of L, a mass of M, a velocity gradient observed along the main axis of the filament of ∇v, and an inclination angle to the plane of sky of α, the rate of mass flow $\dot{M}$ is given by (Kirk et al. 2013)

$$\dot{M} = \frac{|\nabla v|M}{\tan(\alpha)}, \qquad (5)$$

where $|\nabla v|$ is the magnitude of the velocity gradient. Based on our estimates of the branch mass and velocity gradient (above and Section 6.1) and considering a range of plausible inclination angles, we derive mass accretion rates of 1.8×10^{-4} $M_\odot$ yr^{-1} (for $T_{\rm dust} = 25$ K and an inclination angle $\alpha = 60°$) to 1.2×10^{-3} $M_\odot$ yr^{-1} ($T_{\rm dust} = 15$ K and $\alpha = 30°$).

We note that in addition to the uncertainties in inclination angle and dust temperature reflected in the range quoted above, our estimates of $\dot{M}$ are also affected by other sources of uncertainty in our mass estimates. We estimate a factor of $\sim$2 systematic uncertainty, encompassing the uncertainties in the adopted κ and gas-to-dust mass ratio and the uncertainty associated with the isothermal assumption (see also e.g. Brogan et al. 2009; Beuther et al. 2021). While assuming optically thin dust emission can lead to underestimating masses on core scales (e.g. Cyganowski et al. 2014; Brogan et al. 2016), the optically thin assumption is likely to be valid over the vast majority of the area of Branch 8, which has a mean brightness temperature[9] of only 0.35 K (see also e.g. Beuther et al. 2018). We also note that we have not attempted to impose a boundary between 0.82-mm continuum emission associated with the filament and with the MM2 core. The integrated flux density reported for MM2 in Section 3.1 is a fit to the total emission at the core position, so includes a contribution from the background filament, and our measurement of the integrated flux density of Branch 8 includes the area of the compact core.

Reported mass accretion rates along filaments vary by two orders of magnitude, from $\sim 10^{-5}$ $M_\odot$ yr^{-1} (e.g. Kirk et al. 2013; Henshaw et al. 2014; Peretto et al. 2014; Treviño-Morales et al. 2019; Li et al. 2022) to $\sim 10^{-4}$ $M_\odot$ yr^{-1} (e.g. Lu et al. 2018; Yuan et al. 2018; Chen et al. 2019) to $\sim 10^{-3}$ $M_\odot$ yr^{-1} (e.g. Liu et al. 2016; Hu et al. 2021). This range is likely attributable to the different total masses of these star-forming regions (e.g. low-mass or high-mass) combined with variations in velocity gradient measurements (e.g. tracer, spatial scale), mass calculations (e.g. based on molecular line or dust emission, clump mass or filament mass), and inclination angle

---

[8]Henshaw et al. (2014) interpret the symmetrical velocity gradients (with a mean magnitude of $\sim$2.5 km s^{-1} pc^{-1}) towards the SW core in IRDC G035.39-00.33 as either accretion flows along filaments towards the SW core, or an expanding shell of dense gas driven by protostellar outflows and/or stellar winds. The expanding shell scenario is supported by the detection of 8 and 24 μm emission (indicative of the presence of young stars) and a high-velocity redshifted wing traced by CO (1-0) (indicative of protostellar outflows) towards the SW core. As introduced in Section 1, MM2 hosts an early-stage high-mass protobinary system that drives a low-velocity bipolar outflow. Compared with the SW core, MM2 is on an earlier evolutionary stage; its protostellar feedback is thus less likely to drive an expanding shell of dense gas with a velocity gradient of $\sim$10.5 km s^{-1} pc^{-1}, which is higher than that reported by Henshaw et al. (2014) by a factor of $\sim$4. In addition, the observed $\sim$south–north velocity gradient in Branch 8 is unlikely to be caused by the $\sim$west–east bipolar outflow associated with MM2 (see Fig. 7).

[9]Measured from the brightness temperature map computed using the beam-size and the tt.brightnessImage function of toddTools.
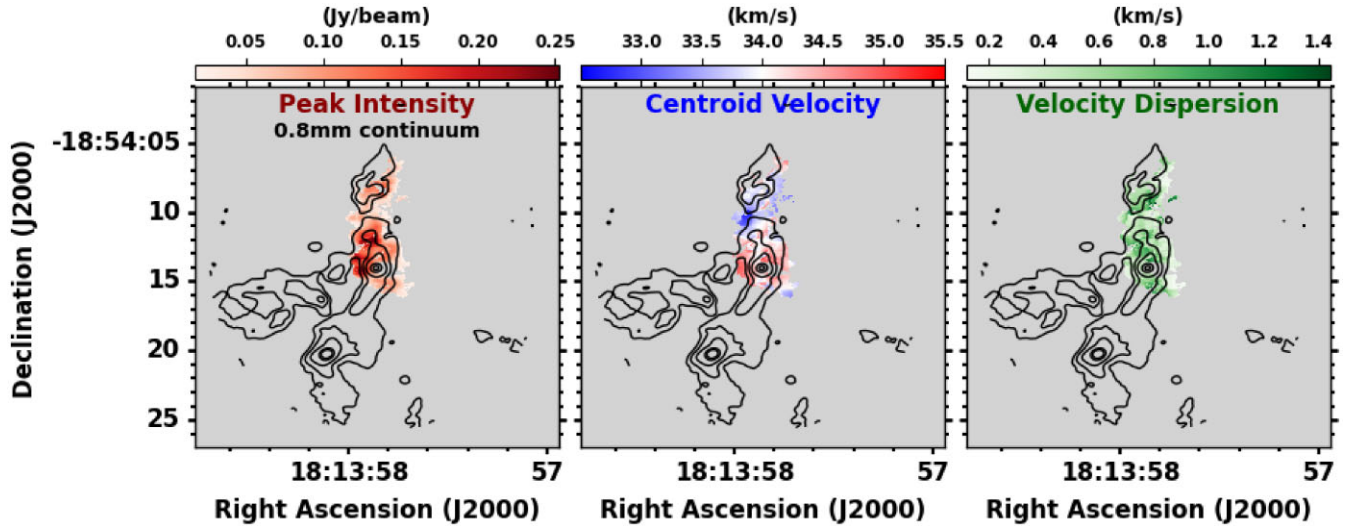
Figure 12. Left panel: distribution of peak intensities of the velocity components of Tree 9. Middle panel: centroid velocity map of Tree 9. Right panel: velocity dispersion map of Tree 9. ALMA 0.82-mm continuum contours (black, levels: 0.5mJy beam^{-1} × [5, 15, 40, 160, 280]) are overlaid in all panels.

assumptions. Our estimated $\dot{M}$ of 1.8×10^{-4} to 1.2×10^{-3} M$_\odot$ yr^{-1} is higher than the values reported in early studies of filamentary accretion flows in high-mass IRDCs [$\sim$(2.5–7)$\times 10^{-5}$ M$_\odot$ yr^{-1}, e.g. Henshaw et al. 2014; Peretto et al. 2014]. The typical accretion rates of (0.5–3.5) $\times 10^{-4}$ M$_\odot$ yr^{-1} found by Lu et al. (2018) in their study of NH$_3$ filaments in high-mass star-forming clouds also fall at the low end of our estimated range. We note that our estimated velocity gradient is also higher ($\sim$ 10.5 km s^{-1} pc^{-1} compared to $\sim$ 1–2.5 km s^{-1} pc^{-1} for the clouds studied by Henshaw et al. 2014; Peretto et al. 2014; Lu et al. 2018), which would naturally lead to higher estimated accretion rates for filaments of roughly comparable mass (equation 5). Liu et al. (2016) report a similarly large velocity gradient ($\sim$10 km s^{-1} pc^{-1}) in filaments identified in NH$_3$(1,1) in the high-mass cluster-forming region AFGL 5142. Adopting the clump mass as a lower limit to the total mass of filaments, Liu et al. (2016) derive a filamentary mass accretion rate of $\sim 2.1 \times 10^{-3}$ M$_\odot$ yr^{-1}, within a factor of 2 of the high end of our estimates for G11.92−0.61 MM2.

6.3 Multiple filamentary accretion flows

In addition to Tree 0, Tree 9 also displays a velocity gradient along the main filamentary structure in an $\sim$north–south direction. Fig. 12 shows maps of the spatial distribution of the peak intensities, centroid velocities, and velocity dispersions of the velocity components in Tree 9 (as shown for Tree 0 in Fig. 9). The maximum peak intensity in Tree 9 is 252.1 mJy beam^{-1} and the median is 75.0 mJy beam^{-1}. The centroid velocities of the components in Tree 9 fall within the lower velocity of the two main peaks in Fig. 5, ranging from 32.7 to 35.2 km s^{-1} with a median of 34.0 km s^{-1} (in contrast to Tree 0, see Section 5.2). The maximum velocity dispersion in Tree 9 is 1.4 km s^{-1} and the median is 0.5 km s^{-1}. Though the brightest components of Tree 0 are about a factor of 2 stronger than those of Tree 9, the maximum and median velocity dispersions of the two trees are similar. Notably, the distinct centroid velocity ranges of the two trees (32.7–35.2 km s^{-1} for Tree 9 and 35.0–38.8 km s^{-1} for Tree 0) suggest that they are kinematically separate structures. We measure the velocity gradient of Tree 9 following the procedure described in Section 6.1, and obtain a velocity gradient with a magnitude of

$\sim$9.0 km s^{-1}pc^{-1} and a direction of $\sim$149° (east of north). If the structure traced by Tree 9 is oriented such that its northern end is further from the observer than its southern end, the observed velocity gradient is consistent with a stream of gas flowing towards MM2. The distinct ranges of centroid velocities and the comparable velocity dispersions of Tree 0 and Tree 9 suggest a scenario in which MM2 is fed by multiple filamentary gas flows that partially overlap along the line of sight. This implies that the filamentary structure seen in the 0.82-mm dust continuum contains multiple kinematic substructures.

Velocity-coherent substructures within filaments (often known as 'fibres') have been identified in other high-mass star-forming regions, including Orion (where Hacar et al. 2018 identified 55 position- and velocity-coherent fibres within the integral-shaped filament using N$_2$H$^+$ (1-0)), NGC 6334 (Shimajiri et al. 2019b; Li et al. 2022) and the DR21 ridge in Cygnus X (Cao et al. 2022). Hydrodynamic simulations with turbulence can reproduce filament substructures similar to those seen in observations, and demonstrate that they play a crucial role in channelling mass on to star-forming cores embedded within filaments (e.g. Smith, Glover & Klessen 2014; Smith et al. 2016; Clarke, Williams & Walch 2020). However, simulation-based studies of the correspondence between fibres identified in position–position–velocity space and coherent substructures in position–position–position space have also emphasized the need for caution in interpreting observed filament substructures due to line-of-sight confusion and projection effects (e.g. Zamora-Avilés, Ballesteros-Paredes & Hartmann 2017 and Clarke et al. 2018, with the latter analysing synthetic C^{18}O observations).

7 DISCUSSION

7.1 Mass inflow feeding the protobinary

Our analysis of the gas kinematics in the surroundings of MM2 reveals position- and velocity-coherent substructures in the N$_2$H$^+$-emitting gas that we interpret as tracing filamentary accretion flows on to MM2 (Section 6). As MM2 is now known to host a young protobinary system undergoing ongoing accretion (Section 1, see also Cyganowski et al. 2022), we can use our estimates of the filamentary mass inflow rate to consider the time-scales for filament-

fed growth of the embedded protostars. Cyganowski et al. (2022) estimate the current protostellar masses of the binary members to be $\sim 1 M_\odot$ each. If the overall efficiency factor for transporting the gas carried by the filamentary inflows on to the protostars is 50 per cent, the members of the protobinary will double their masses in $\sim 3.3 \times 10^3$ to $\sim 2.2 \times 10^4$ yr (where the range corresponds to the range in our estimated filamentary accretion rate: 1.8×10^{-4} to $1.2 \times 10^{-3} \, M_\odot \, yr^{-1}$, Section 6.2), comparable to the dynamical time-scale of the CH_3OH outflow ($t_{dyn} \sim 4600$ and $12\,100$ yr for the blue and red lobes, respectively; Cyganowski et al. 2022). Similarly, the time for each member of the protobinary to reach a mass of $8 \, M_\odot$ would be $\sim 2.3 \times 10^4$ to $\sim 1.6 \times 10^5$ yr, and the time for each member of the protobinary to reach $10 \, M_\odot$ would be $\sim 3.0 \times 10^4$ to $\sim 2.0 \times 10^5$ yr. Interestingly, using chemical clocks, Sabatini et al. (2021) derive time-scales of $\sim 5 \times 10^4$ yr for the 70μm-weak phase and of $\sim 1.2 \times 10^5$ yr for the subsequent MIR-weak phase in the evolutionary stages of the ATLASGAL-TOP100 sample of massive star-forming clumps (König et al. 2017). While the uncertainties are considerable, we note that the combined time-scale of the 70 μm-weak and MIR-weak phases ($\sim 1.7 \times 10^5$ yr) is comparable to our upper estimates of the time-scale for the binary members to become massive protostars ($M \gtrsim 8 \, M_\odot$).

We note that the time-scale estimates above consider mass aggregation processes involving multiple spatial scales: (a) from filaments to cores and (b) from cores to stars. The efficiencies of both processes are poorly constrained. Analysis of the relationship between the prestellar core population and the column density shows that only a small fraction of dense gas is contained in prestellar cores, for example, ~ 15 per cent in the Aquila Cloud Complex (André et al. 2014) and ~ 22 per cent in Orion B (Könyves et al. 2020). In the GHC scenario, filaments themselves are assembling mass from their surroundings while they transport material on to embedded star-forming cores (Vázquez-Semadeni et al. 2017, 2019). The efficiency of the mass transport from filaments to cores will depend on the dynamical time-scales of the two structures.

7.2 Velocity gradient across filament

The direction of the best-fitting velocity gradient for the centroid velocity map of Branch 8 is $\sim 19°$ east of north, offset by $\sim 40°$ from the main axis of Branch 8 (see top right panel of Fig. 11). This offset suggests that the observed velocity gradient consists of a component that is aligned parallel to the main axis of Branch 8 ($\sim$southeast–northwest) and a perpendicular component ($\sim$southwest–northeast). As discussed above, the parallel component is most likely associated with longitudinal filamentary accretion flows towards MM2. Velocity gradients that are perpendicular to the main axes of filamentary structures have been observed in (sub)filaments in nearby (Kirk et al. 2013; Palmeirim et al. 2013; Fernández-López et al. 2014; Dhabal et al. 2018, 2019; Chen et al. 2020a, 2020b) and high-mass (Schneider et al. 2010; Beuther et al. 2015, Williams et al. 2018; Zhou et al. 2021) star-forming regions. These perpendicular velocity gradients have been interpreted as signatures of asymmetric mass accretion flows on to (sub)filaments (Palmeirim et al. 2013; Chen et al. 2020b), which can be induced by the compression of shocked gas (Dhabal et al. 2018; Shimajiri et al. 2019a; Chen et al. 2020a), as direct results of compression flows (Schneider et al. 2010; Williams et al. 2018; Dhabal et al. 2019; Zhou et al. 2021), and as the combined result of mergers/collisions of velocity-coherent subfilaments and the accretion and rotation of filaments (Beuther et al. 2015).

As G11.92–0.61 is a young embedded massive protocluster where UCHII and H II regions have not yet developed (Ilee et al. 2016) and is

located ~ 1 pc away from the ultracompact H II region G11.94–00.62 (Churchwell, Walmsley & Wood 1992), the kinematics of dense filamentary structures in G11.92–0.61 will not yet be shaped by the feedback from either internal or external expanding H II regions. Branch 8 has a mass of ~ 30–$65 \, M_\odot$ and a length of ~ 0.17pc, yielding a mass per unit length of $M_{line} \approx 174$–$380 \, M_\odot \, pc^{-1}$. These values are higher than the thermal critical values $M_{line,crit}$ calculated with equation (11) of Kirk et al. (2013) for $T \sim 15$–25 K by a factor of ~ 4–15, suggesting that thermal pressure is insufficient to support Branch 8 against gravitational collapse. Branch 8 thus is likely to undergo radial collapse, which, if asymmetric, can also contribute to the observed perpendicular velocity gradient. We speculate that the perpendicular velocity gradient could be the combined result of the radial collapse, mass accretion, and rotation of the filamentary structure, while accretion may dominate over rotation as it evolves (e.g. Kirk et al. 2013). This is a picture consistent with the GHC scenario (Vázquez-Semadeni et al. 2017, 2019), where the mass aggregation processes of filaments and of the cores within them take place concurrently. In this scenario, gas is accreted on to filaments and then continuously flows along them, as posited by Chen et al. (2020b) based on their NH_3 observations of NGC 1333.

7.3 Limitations and future work

We note that the line profiles in the N_2H^+(4-3) data cube are shaped by three main factors: multiple velocity components, hyperfine structure (hfs), and missing short spacing information. In addition, self-absorption might also affect the line profiles in the densest region. In this work, we have used Gaussian Decomposition to disentangle the multiple velocity components and study the gas kinematics. Of the remaining factors, we can quantitatively investigate the effects of hfs and self-absorption using our existing data, while missing short spacings are an area for future work, as discussed below.

As noted in Section 3.2.2, the hfs of the N_2H^+ (4-3) transition can contribute to shaping the line profile (see also Pagani et al. 2009) and Friesen et al. (2010) found that Gaussian-fitting overestimated the intrinsic N_2H^+ line width by ~ 10-25 per cent. To quantify this effect in our data, we carry out multicomponent hfs fitting for a selection of 10 spectra using pyspeckit (Ginsburg & Mirocha 2011; Ginsburg et al. 2022). The spectra were selected to span a range in the number of fitted Gaussian components (from 1 to 5); their locations are marked in the right-hand panel of Fig. 4. The PYSPECKIT package applies a uniform excitation temperature (T_{ex}) to all fitted hyperfine lines. A one-component hfs fit thus has four free parameters: the centroid velocity, the velocity dispersion, T_{ex}, and the optical depth τ. An example of a one-component hfs fit is shown in Fig. 13. Since the number of fitted parameters in a multicomponent hfs fit is $4\times$ the number of velocity components, we use the best-fitting Gaussian models as initial guesses for the centroid velocity and the velocity dispersion to better constrain the hfs fitting. This approach achieves good fits for spectra with one or two velocity components identified by Gaussian decomposition, but T_{ex} and τ are poorly constrained for many components in more complex spectra. To obtain reasonable fits for these more complex cases, we fix T_{ex} for poorly constrained components to the mean value from the initial good fits (14 K). Fig. 14 presents a comparison of the results of our Gaussian decomposition and hyperfine structure fitting for the selected spectra. In this limited sample, we find that in our data Gaussian Decomposition can overestimate the line width by 37 per cent on average, while the fitted centroid velocities are consistent to within 0.1 per cent.
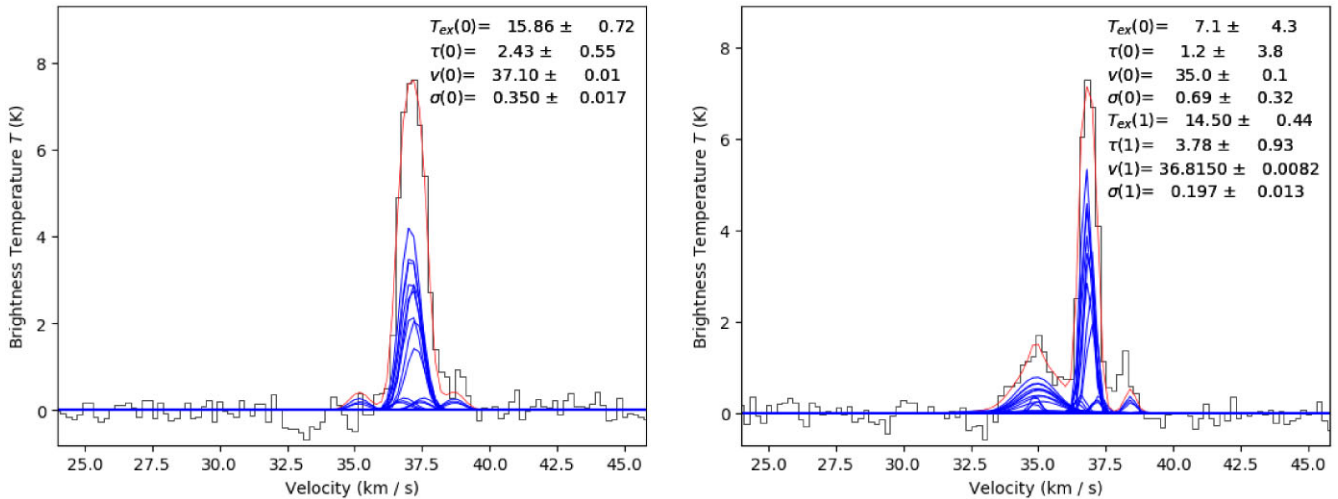
Figure 13. Examples of one-component (left panel) and two-component (right panel) $N_2H^+(4-3)$ hyperfine structure fits (red) overlaid on the observed spectra (black). The individual hyperfine components are shown in blue. The best-fitting parameters are listed at top right in each panel.
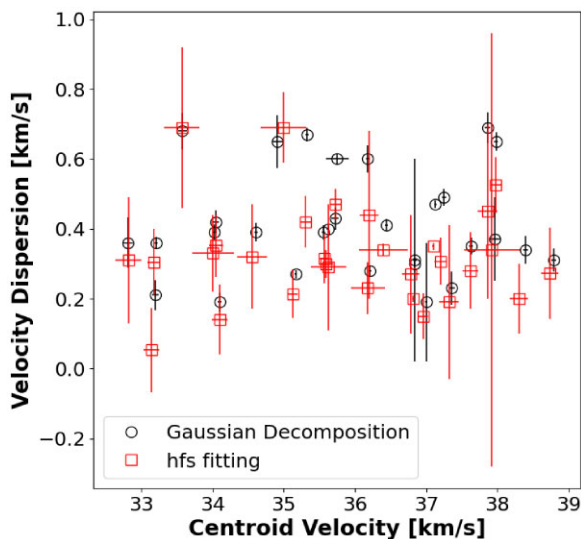
Figure 14. Comparison of fitted parameters from Gaussian decomposition (black circles) and hyperfine structure fitting (red squares) for selected spectra (see Section 7.3).

The hfs fits can also be used to investigate the optical depth of the N_2H^+ emission, and so the potential effects of self-absorption. Inspecting the aforementioned initial good hfs fits, we see no indications of self-absorption in the line profiles for components with moderate optical depths >1 (e.g. the components with $\tau \sim 2-4$ in Fig. 13). As the multicomponent hfs fits are in general poorly constrained, we use the radiative transfer code RADEX (van der Tak et al. 2007) to estimate the optical depth for all velocity components fit in our SCOUSEPY analysis. We use the molecular data and collisional rate coefficients for N_2H^+ from the Leiden Atomic and Molecular Database (Schöier et al. 2005); the collisional rate coefficients are for N_2H^+ (including hfs) in collisions with H_2 for a temperature range of 5–2000 K, and are extrapolated and scaled from those for N_2H^+ in collisions with He (Daniel et al. 2005). The other required inputs to RADEX are the H_2 density n_{H_2}, the gas kinetic temperature T_{kin}, the line width (FWHM), the molecular column density $N(N_2H^+)$, and the background temperature T_{bg}. The mean gas density of

Branch 8 is estimated to be $n_{H_2} \sim (1-3) \times 10^6$ cm^{-3} assuming a cylinder with a height of ~ 0.17 pc, a diameter of ~ 0.05 pc, and a mass of $\sim 30-65$ M$_\odot$ (see Section 6). The N_2H^+ column density is estimated following equation A4 in Caselli et al. (2002), using the integrated intensity of each fitted velocity component and $T_{ex} = 14$ K (see the previous paragraph). The partition function for $T_{ex} = 14$ K is interpolated using values from the Cologne Database for Molecular Spectroscopy (CDMS, Müller et al. 2001, 2005). We estimate the optical depth for each fitted velocity component using the N_2H^+ column density estimated as described above, the fitted velocity dispersion converted to FWHM line width, $n_{H_2} = 10^6$ cm^{-3}, $T_{bg} = 2.73$ K, and $T_{kin} = 15-25$ K (see Section 6.2) using the PYTHON package SPECTRALRADEX[10] (Holdship et al. 2021). From this analysis, we find that the optical depth of the hyperfine line $(JF_1F) = (456 - 345)$, the strongest hyperfine line with the largest optical depth, ranges from 0.02 to 1.5 for $T_{kin} = 15$ K and from 0.03 to 2.2 for $T_{kin} = 25$ K. The total optical depth of the N_2H^+ (4-3) transition ranges from 0.1 to 7.2 for $T_{kin} = 15$ K, with ~ 99 per cent of fitted components having $\tau < 4$, and from 0.2 to 11 for for $T_{kin} = 25$ K, with ~ 93 per cent of fitted components having $\tau < 4$. We emphasize that the optical depths estimated from our RADEX modelling are sensitive to the assumed T_{kin} and n_{H_2} and to the column density, which depends on the assumed T_{ex} (for example, for the single-component spectrum shown in the left-hand panel of Fig. 13, our RADEX modelling yields a total optical depth of 3.0 for $T_{kin} = 15$ K and 4.8 for $T_{kin} = 25$ K, compared to 2.4 from the hfs fit) and that T_{ex}, T_{kin}, and n_{H_2} are physically expected to vary spatially, which we cannot constrain with our ALMA data. Notably, the number of fitted velocity components does not track the strength of the N_2H^+ emission (compare Fig. 2b and 4), for example, the number of fitted components is higher to the north of MM2, while the $N_2H^+(4-3)$ emission is strongest to the south. Combined with the generally moderate optical depths, this suggests that self-absorption is not a major contributor to the observed line profiles.

The effects of missing short-spacing information cannot be quantified with existing data (since no short-spacing N_2H^+ (4-3) observations are available) and this is a limitation of this study. Hacar

[10]https://spectralradex.readthedocs.io

et al.[11] have shown that missing short- and zero-spacings can affect the line profiles and relative intensities of the hyperfine components for N_2H^+ (1-0), and that the effects are highly non-linear. However, these effects have not been investigated for N_2H^+ (4-3), and the impacts may be lessened by the much higher E_{upper} and critical density of the (4-3) transition: $E_{upper} = 44.7$ K and $n_{crit} = 2.8 \times 10^6$ cm^{-3} at 20 K for N_2H^+(4-3) compared to $E_{upper} = 4.5$ K and $n_{crit} = 4.1 \times 10^4$ cm^{-3} at 20 K for N_2H^+(1-0).

The most straightforward way to address the lack of short spacing data in this study, and a possible area for future work, would be additional observations of N_2H^+(4-3) towards G11.92−0.61, for example, Atacama Compact Array (ACA) and Total Power (TP) observations. N_2H^+(4-3) observations are, however, challenging and observationally expensive, as the poor atmospheric transmission at the line frequency means that observations require excellent weather and/or very large amounts of observing time. The N_2H^+(4-3) observations presented here total 4.52 h of on-source ALMA 12-m time, for a single pointing (Table 1), and ACA 7-m observations suitable for combining with the existing data would require >20 h on-source[12] Alternately, high-spatial-dynamic-range observations of the G11.92−0.61 region in other lines known to trace filamentary accretion flows (e.g. lower J transitions of N_2H^+ or lines of NH_3 or $H^{13}CO$; Hacar et al. 2018; Chen et al. 2020b; Cao et al. 2022) may offer a more practical path to confirming our results with additional observations and further investigating kinematics and multiscale mass accretion in the G11.92−0.61 region.

8 CONCLUSIONS

We have observed the former high-mass prestellar core candidate MM2, which has recently been revealed to host a protobinary system driving a low-velocity CH_3OH outflow. Our deep, sub-arcsecond (∼2000 au) resolution ALMA observations targeted the dense and depleted gas tracers H_2D^+(1_1, 0-1_1, 1) and N_2H^+(4-3). Our main findings are summarized as follows:

(i) MM2, which appears as a strong, compact source of 0.82-mm continuum emission, lies on an ∼north–south filamentary structure within the G11.92−0.61 massive protocluster. The filament is traced by both 0.82 mm continuum and N_2H^+ (4-3) emission, but there are differences in the morphologies of the two tracers, with the peaks of the integrated N_2H^+ emission offset by 0.9 and 1.2 arcsec (∼3000 and 4000 au) from the 0.82-mm continuum peak.

(ii) H_2D^+ is undetected towards MM2, to 4σ limits of 10.8 mJy beam^{-1}/0.23 K. The non-detection of H_2D^+ is likely due to internal heating from the recently discovered protobinary system.

(iii) The N_2H^+ spectra are complex, with multiple emission peaks and, towards the MM2 core, absorption features. The complexity and spatial variation of the N_2H^+ spectra indicate that multiple velocity components are present along the line of sight.

(iv) Our analysis of the N_2H^+ gas kinematics, using pixel-by-pixel Gaussian decomposition with SCOUSEPY and hierarchical clustering of the extracted velocity components with ACORNS, reveals a hierarchical system in the N_2H^+-emitting gas comprised of 70 velocity- and position-coherent clusters, known as 'trees'. The eight largest trees describe >60 per cent of the fitted velocity components, with ∼20 per cent of fitted velocity components in the largest (primary) tree.

(v) The primary tree exhibits an ∼north–south velocity gradient along the filamentary structure traced by the 0.82-mm continuum emission. Analysing an ∼0.17 pc-long substructure within this tree to focus on gas kinematics around MM2, we find a best-fitting velocity gradient of ∼10.5 km s^{-1} pc^{-1}. Interpreting this velocity gradient as tracing filamentary accretion flows towards MM2, we estimate a mass inflow rate of ∼ 1.8×10^{-4} to ∼ 1.2×10^{-3} M$_\odot$ yr^{-1}.

Our analysis of the dense gas kinematics in the surroundings of MM2 indicates that rather than being an isolated core, MM2 is connected to its larger scale environment. In particular, the ongoing accretion on to the protobinary system – indicated by its outflow activity – is likely fed by the larger scale filamentary accretion flows. If 50 per cent of the mass inflow estimated above reaches the protostars, each will reach a mass of 8 M$_\odot$ within ∼ 1.6×10^5 yr, which is intriguingly comparable to the combined time-scale of the 70μm-weak + MIR-weak phases of high-mass star formation estimated from chemical clocks (e.g. Sabatini et al. 2021). In addition to the primary tree that is the focus of our analysis, we also identify a velocity gradient consistent with a filamentary accretion flow on to MM2 in a second tree, which is kinematically distinct but partially overlaps the primary tree on the plane of the sky. This finding suggests that the filamentary dust continuum structure contains multiple kinematic substructures, and that MM2 may be fed by multiple filamentary accretion flows. Additional observations of the G11.92−0.61 region, including in lower J and more easily observed N_2H^+ transitions, are needed to explore this possibility and expand the investigation of mass accretion in G11.92−0.61 to larger spatial scales.

---

[11]Hacar, A., The need for data combination in the ALMA era, EAS2020–SS13a: 8 yr of ALMA ground-breaking results: a joint venture between the ALMA user community and the ALMA Regional Centres, 2020 June 29–July 3.

[12]Based on the time multipliers in the ALMA Cycle 10 Proposer's Guide, https://almascience.eso.org/proposing/proposers-guide.

PYTHON, Robitaille & Bressert 2012), and ANALYSISUTILS (Hunter et al. 2023).

DATA AVAILABILITY

The ALMA 0.82-mm continuum image and N_2H^+ (4-3) and $H_2D^+(1_{1,0}-1_{1,1})$ line cubes are available at https://doi.org/10.5281/zenodo.12640479.

REFERENCES

Anderson M. et al., 2021, MNRAS, 508, 2964

André P., Di Francesco J., Ward-Thompson D., Inutsuka S. I., Pudritz R. E., Pineda J. E., 2014, in Beuther H., Klessen R. S., Dullemond C. P., Henning T.eds, Protostars and Planets VI. University of Arizona Press, Tucson, AZ. p. 27

André P. et al., 2016, A&A, 592, A54

Astropy Collaboration et al., 2022, ApJ, 935, 167

Bally J., Langer W. D., Stark A. A., Wilson R. W., 1987, ApJ, 312, L45

Barnes A. T. et al., 2023, A&A, 675, A53

Beltrán M. T., Rivilla V. M., Kumar M. S. N., Cesaroni R., Galli D., 2022, A&A, 660, L4

Beuther H., Ragan S. E., Johnston K., Henning T., Hacar A., Kainulainen J. T., 2015, A&A, 584, A67

Beuther H. et al., 2018, A&A, 617, A100

Beuther H. et al., 2021, A&A, 649, A113

Blake G. A., Sandell G., van Dishoeck E. F., Groesbeck T. D., Mundy L. G., Aspin C., 1995, ApJ, 441, 689

Bonnell I. A., Bate M. R., 2006, MNRAS, 370, 488

Bonnell I. A., Bate M. R., Clarke C. J., Pringle J. E., 2001, MNRAS, 323, 785

Bonnell I. A., Bate M. R., Vine S. G., 2003, MNRAS, 343, 413

Bonnell I. A., Vine S. G., Bate M. R., 2004, MNRAS, 349, 735

Bonnell I. A., Clark P., Bate M. R., 2008, MNRAS, 389, 1556

Bonnell I. A., Dobbs C. L., Smith R. J., 2013, MNRAS, 430, 1790

Bontemps S., Motte F., Csengeri T., Schneider N., 2010, A&A, 524, A18

Breen S. L., Ellingsen S. P., 2011, MNRAS, 416, 178

Brogan C. L., Hunter T. R., Cyganowski C. J., Indebetouw R., Beuther H., Menten K. M., Thorwirth S., 2009, ApJ, 707, 1

Brogan C. L., Hunter T. R., Cyganowski C. J., Friesen R. K., Chandler C. J., Indebetouw R., 2011, ApJ, 739, L16

Brogan C. L., Hunter T. R., Cyganowski C. J., Chandler C. J., Friesen R., Indebetouw R., 2016, ApJ, 832, 187

Busquet G. et al., 2013, ApJ, 764, L26

Butler M. J., Tan J. C., 2009, ApJ, 696, 484

Butler M. J., Tan J. C., 2012, ApJ, 754, 5

Cao Y., Qiu K., Zhang Q., Li G.-X., 2022, ApJ, 927, 106

Caselli P., Ceccarelli C., 2012, A&AR., 20, 56

Caselli P., Walmsley C. M., Zucconi A., Tafalla M., Dore L., Myers P. C., 2002, ApJ, 565, 344

Caselli P., van der Tak F. F. S., Ceccarelli C., Bacmann A., 2003, A&A, 403, L37

Caselli P., Vastel C., Ceccarelli C., van der Tak F. F. S., Crapsi A., Bacmann A., 2008, A&A, 492, 703

Ceccarelli C., Caselli P., Bockelée-Morvan D., Mousis O., Pizzarello S., Robert F., Semenov D., 2014, in Beuther H., Klessen R. S., Dullemond C. P., Henning T.eds, Protostars and Planets VI. University of Arizona Press, Tucson, AZ. p. 859

Chen H.-R. V. et al., 2019, ApJ, 875, 24

Chen C.-Y., Mundy L. G., Ostriker E. C., Storm S., Dhabal A., 2020a, MNRAS, 494, 3675

Chen M. C.-Y. et al., 2020b, ApJ, 891, 84

Churchwell E., Walmsley C. M., Wood D. O. S., 1992, A&A, 253, 541

Clarke S. D., Whitworth A. P., Spowage R. L., Duarte-Cabral A., Suri S. T., Jaffa S. E., Walch S., Clark P. C., 2018, MNRAS, 479, 1722

Clarke S. D., Williams G. M., Walch S., 2020, MNRAS, 497, 4390

Commerçon B., Hennebelle P., Henning T., 2011, ApJ, 742, L9

Cortes P., et al. 2023, ALMA Cycle 10 Technical Handbook, Zenodo. Available at: https://doi.org/10.5281/zenodo.7822943

Cunningham A. J., Klein R. I., Krumholz M. R., McKee C. F., 2011, ApJ, 740, 107

Cyganowski C. J. et al., 2008, AJ, 136, 2391

Cyganowski C. J., Brogan C. L., Hunter T. R., Churchwell E., 2009, ApJ, 702, 1615

Cyganowski C. J., Brogan C. L., Hunter T. R., Churchwell E., Zhang Q., 2011a, ApJ, 729, 124

Cyganowski C. J., Brogan C. L., Hunter T. R., Churchwell E., 2011b, ApJ, 743, 56

Cyganowski C. J., Koda J., Rosolowsky E., Towers S., Donovan Meyer J., Egusa F., Momose R., Robitaille T. P., 2013, ApJ, 764, 61

Cyganowski C. J. et al., 2014, ApJ, 796, L2

Cyganowski C. J., Brogan C. L., Hunter T. R., Smith R., Kruijssen J. M. D., Bonnell I. A., Zhang Q., 2017, MNRAS, 468, 3694

Cyganowski C. J., Ilee J. D., Brogan C. L., Hunter T. R., Zhang S., Harries T. J., Haworth T. J., 2022, ApJ, 931, L31

Dale J. E., Bonnell I., 2011, MNRAS, 414, 321

Dale J. E., Ercolano B., Bonnell I. A., 2012, MNRAS, 424, 377

Daniel F., Dubernet M. L., Meuwly M., Cernicharo J., Pagani L., 2005, MNRAS, 363, 1083

Daniel F., Cernicharo J., Dubernet M. L., 2006, ApJ, 648, 461

Dewangan L. K., Ojha D. K., Baug T., 2017, ApJ, 844, 15

Dewangan L. K., Ojha D. K., Sharma S., Palacio S. d., Bhadari N. K., Das A., 2020, ApJ, 903, 13

Dhabal A., Mundy L. G., Rizzo M. J., Storm S., Teuben P., 2018, ApJ, 853, 169

Dhabal A., Mundy L. G., Chen C.-y., Teuben P., Storm S., 2019, ApJ, 876, 108

Dobbs C. L., Bonnell I. A., Clark P. C., 2005, MNRAS, 360, 2

Duarte-Cabral A., Bontemps S., Motte F., Hennemann M., Schneider N., André P., 2013, A&A, 558, A125

Duarte-Cabral A., Bontemps S., Motte F., Gusdorf A., Csengeri T., Schneider N., Louvet F., 2014, A&A, 570, A1

Federrath C., 2013, MNRAS, 436, 1245

Federrath C. et al., 2016, ApJ, 832, 143

Fernández-López M. et al., 2014, ApJ, 790, L19

Friesen R. K., Di Francesco J., Myers P. C., Belloche A., Shirley Y. L., Bourke T. L., André P., 2010, ApJ, 718, 666

Friesen R. K., Di Francesco J., Bourke T. L., Caselli P., Jørgensen J. K., Pineda J. E., Wong M., 2014, ApJ, 797, 27

Ginsburg A., Mirocha J., 2011, Astrophysics Source Code Library, record ascl:1109.001

Ginsburg A., Sokolov V., de Val-Borro M., Rosolowsky E., Pineda J. E., Sipőcz B. M., Henshaw J. D., 2022, AJ, 163, 291

Gómez G. C., Vázquez-Semadeni E., 2014, ApJ, 791, 124

Goodman A. A., Benson P. J., Fuller G. A., Myers P. C., 1993, ApJ, 406, 528

Goodman A. A., Rosolowsky E. W., Borkin M. A., Foster J. B., Halle M., Kauffmann J., Pineda J. E., 2009, Nature, 457, 63

Hacar A., Alves J., Tafalla M., Goicoechea J. R., 2017, A&A, 602, L2

Hacar A., Tafalla M., Forbrich J., Alves J., Meingast S., Grossschedl J., Teixeira P. S., 2018, A&A, 610, A77

Harris C. R. et al., 2020, Nature, 585, 357

Hennemann M. et al., 2012, A&A, 543, L3

Henshaw J. D., Caselli P., Fontani F., Jiménez-Serra I., Tan J. C., Hernandez A. K., 2013, MNRAS, 428, 3425

Henshaw J. D., Caselli P., Fontani F., Jiménez-Serra I., Tan J. C., 2014, MNRAS, 440, 2860

Henshaw J. D. et al., 2016, MNRAS, 457, 2675

Henshaw J. D. et al., 2017, MNRAS, 464, L31

Henshaw J. D. et al., 2019, MNRAS, 485, 2457

Hofner P., Churchwell E., 1996, A&AS, 120, 283

Holdship J. et al., 2021, A&A, 654, A55

Hu B. et al., 2021, ApJ, 908, 70

Hunter J. D., 2007, Comput. Sci. Eng., 9, 90

Hunter T. R., Brogan C. L., Cyganowski C. J., Schnee S., 2015, in Simon R., Schaaf R., Stutzki J., eds, EAS Publications Series Vol. 75-76, Conditions and Impact of Star Formation. ESA, Noordwijk, p.285

Hunter T. R., Petry D., Barkats D., Corder S., Indebetouw R., 2023, analysisUtils, Zenodo, Available at: https://doi.org/10.5281/zenodo.7502160

Ilee J. D., Cyganowski C. J., Nazari P., Hunter T. R., Brogan C. L., Forgan D. H., Zhang Q., 2016, MNRAS, 462, 4386

Ilee J. D., Cyganowski C. J., Brogan C. L., Hunter T. R., Forgan D. H., Haworth T. J., Clarke C. J., Harries T. J., 2018, ApJ, 869, L24

Jackson J. M., Finn S. C., Chambers E. T., Rathborne J. M., Simon R., 2010, ApJ, 719, L185

Kainulainen J., Ragan S. E., Henning T., Stutz A., 2013, A&A, 557, A120

Kauffmann J., Pillai T., 2010, ApJ, 723, L7

Keown J. et al., 2019, ApJ, 884, 4

Kirk H., Myers P. C., Bourke T. L., Gutermuth R. A., Hedden A., Wilson G. W., 2013, ApJ, 766, 115

Kong S. et al., 2016, ApJ, 821, 94

Kong S., Tan J. C., Caselli P., Fontani F., Liu M., Butler M. J., 2017, ApJ, 834, 193

Kong S., Arce H. G., Tobin J. J., Zhang Y., Maureira M. J., Kratter K. M., Pillai T. G. S., 2023, ApJ, 950, 187

König C. et al., 2017, A&A, 599, A139

Könyves V. et al., 2020, A&A, 635, A34

Koumpia E., Evans L., Di Francesco J., van der Tak F. F. S., Oudmaijer R. D., 2020, A&A, 643, A61

Krumholz M. R., Klein R. I., McKee C. F., Offner S. S. R., Cunningham A. J., 2009, Science, 323, 754

Kuiper R., Hosokawa T., 2018, A&A, 616, A101

Kuiper R., Yorke H. W., Turner N. J., 2015, ApJ, 800, 86

Kumar M. S. N., Palmeirim P., Arzoumanian D., Inutsuka S. I., 2020, A&A, 642, A87

Li S. et al., 2022, ApJ, 926, 165

Lindner R. R. et al., 2015, AJ, 149, 138

Liu T. et al., 2016, ApJ, 824, 31

Liu H.-L. et al., 2023, MNRAS, 522, 3719

Lu X. et al., 2018, ApJ, 855, 9

McKee C. F., Tan J. C., 2002, Nature, 416, 59

McKee C. F., Tan J. C., 2003, ApJ, 585, 850

Ma Y., Zhou J., Esimbek J., Ji W., Wu G., Yuan Y., 2013, Ap&SS, 345, 297

Maschberger T., Clarke C. J., Bonnell I. A., Kroupa P., 2010, MNRAS, 404, 1061

Miettinen O., 2012a, A&A, 540, A104

Miettinen O., 2012b, A&A, 542, A101

Miettinen O., 2020, A&A, 634, A115

Mignon-Risse R., González M., Commerçon B., 2021, A&A, 656, A85

Molet J. et al., 2019, A&A, 626, A132

Mookerjea B., Veena V. S., Güsten R., Wyrowski F., Lasrado A., 2023, MNRAS, 520, 2517

Müller H. S. P., Thorwirth S., Roth D. A., Winnewisser G., 2001, A&A, 370, L49

Müller H. S. P., Schlöder F., Stutzki J., Winnewisser G., 2005, J. Mol. Struct., 742, 215

Myers P. C., 2009, ApJ, 700, 1609

Myers A. T., McKee C. F., Cunningham A. J., Klein R. I., Krumholz M. R., 2013, ApJ, 766, 97

Nony T. et al., 2018, A&A, 618, L5

Öberg K. I., van Broekhuizen F., Fraser H. J., Bisschop S. E., van Dishoeck E. F., Schlemmer S., 2005, ApJ, 621, L33

Ossenkopf V., Henning T., 1994, A&A, 291, 943

Padoan P., Pan L., Juvela M., Haugbølle T., Nordlund Å., 2020, ApJ, 900, 82

Pagani L., Daniel F., Dubernet M. L., 2009, A&A, 494, 719

Palmeirim P. et al., 2013, A&A, 550, A38

Peretto N., Fuller G. A., 2010, ApJ, 723, 555

Peretto N. et al., 2013, A&A, 555, A112

Peretto N. et al., 2014, A&A, 561, A83

Pillai T., Caselli P., Kauffmann J., Zhang Q., Thompson M. A., Lis D. C., 2012, ApJ, 751, 135

Qi C. et al., 2013, Science, 341, 630

Ragan S. E., Heitsch F., Bergin E. A., Wilner D., 2012, ApJ, 746, 174

Rathborne J. M., Jackson J. M., Simon R., 2006, ApJ, 641, 389

Redaelli E., Bovino S., Giannetti A., Sabatini G., Caselli P., Wyrowski F., Schleicher D. R. G., Colombo D., 2021, A&A, 650, A202

Redaelli E., Bovino S., Sanhueza P., Morii K., Sabatini G., Caselli P., Giannetti A., Li S., 2022, ApJ, 936, 169

Riener M., Kainulainen J., Henshaw J. D., Orkisz J. H., Murray C. E., Beuther H., 2019, A&A, 628, A78

Robitaille T., Bressert E., 2012, Astrophysics Source Code Library, record ascl:1208.017

Rosen A. L., 2022, ApJ, 941, 202

Rosen A. L., Krumholz M. R., 2020, AJ, 160, 78

Rosen A. L., Krumholz M. R., McKee C. F., Klein R. I., 2016, MNRAS, 463, 2553

Rosen A. L., Li P. S., Zhang Q., Burkhart B., 2019, ApJ, 887, 108

Rosolowsky E. W., Pineda J. E., Kauffmann J., Goodman A. A., 2008, ApJ, 679, 1338

Sabatini G. et al., 2021, A&A, 652, A71

Sato M. et al., 2014, ApJ, 793, 72

Schneider N., Csengeri T., Bontemps S., Motte F., Simon R., Hennebelle P., Federrath C., Klessen R., 2010, A&A, 520, A49

Schneider N. et al., 2012, A&A, 540, L11

Schöier F. L., van der Tak F. F. S., van Dishoeck E. F., Black J. H., 2005, A&A, 432, 369

Shimajiri Y., André P., Palmeirim P., Arzoumanian D., Bracco A., Könyves V., Ntormousi E., Ladjelate B., 2019a, A&A, 623, A16

Shimajiri Y., André P., Ntormousi E., Men'shchikov A., Arzoumanian D., Palmeirim P., 2019b, A&A, 632, A83

Smilgys R., Bonnell I. A., 2016, MNRAS, 459, 1985

Smilgys R., Bonnell I. A., 2017, MNRAS, 472, 4982

Smith R. J., Longmore S., Bonnell I., 2009, MNRAS, 400, 1775

Smith R. J., Glover S. C. O., Klessen R. S., 2014, MNRAS, 445, 2900

Smith R. J., Glover S. C. O., Klessen R. S., Fuller G. A., 2016, MNRAS, 455, 3640

Stark R., van der Tak F. F. S., van Dishoeck E. F., 1999, ApJ, 521, L67

Tackenberg J. et al., 2014, A&A, 565, A101

Tan J. C., Kong S., Butler M. J., Caselli P., Fontani F., 2013, ApJ, 779, 96

Tan J. C., Beltrán M. T., Caselli P., Fontani F., Fuente A., Krumholz M. R., McKee C. F., Stolte A., 2014, in Beuther H., Klessen R. S., Dullemond C. P., Henning T.eds, Protostars and Planets VI. University of Arizona Press, Tucson, AZ. p. 149

Tan J. C., Kong S., Zhang Y., Fontani F., Caselli P., Butler M. J., 2016, ApJ, 821, L3

Thwala S. A., Shafi N., Colafrancesco S., Govoni F., Murgia M., 2019, MNRAS, 485, 1938

Tigé J. et al., 2017, A&A, 602, A77

Treviño-Morales S. P. et al., 2019, A&A, 629, A81

van Dishoeck E. F., Phillips T. G., Keene J., Blake G. A., 1992, A&A, 261, L13

van der Tak F. F. S., Caselli P., Ceccarelli C., 2005, A&A, 439, 195

van der Tak F. F. S., Black J. H., Schöier F. L., Jansen D. J., van Dishoeck E. F., 2007, A&A, 468, 627

van't Hoff M. L. R., Walsh C., Kama M., Facchini S., van Dishoeck E. F., 2017, A&A, 599, A101

Vastel C., Caselli P., Ceccarelli C., Phillips T., Wiedner M. C., Peng R., Houde M., Dominik C., 2006, ApJ, 645, 1198

Vasyunin A. I., Semenov D. A., Wiebe D. S., Henning T., 2009, ApJ, 691, 1459

Vázquez-Semadeni E., Gómez G. C., Jappsen A. K., Ballesteros-Paredes J., González R. F., Klessen R. S., 2007, ApJ, 657, 870

Vázquez-Semadeni E., González-Samaniego A., Colín P., 2017, MNRAS, 467, 1313

Vázquez-Semadeni E., Palau A., Ballesteros-Paredes J., Gómez G. C., Zamora-Avilés M., 2019, MNRAS, 490, 3061

Virtanen P. et al., 2020, Nat. Methods, 17, 261
Wang K. et al., 2014, MNRAS, 439, 3275
Wang J.-W., Koch P. M., Galván-Madrid R., Lai S.-P., Liu H. B., Lin S.-J., Pattle K., 2020, ApJ, 905, 158
Williams G. M., Peretto N., Avison A., Duarte-Cabral A., Fuller G. A., 2018, A&A, 613, A11
Xu F.-W. et al., 2023, MNRAS, 520, 3259
Yuan J. et al., 2018, ApJ, 852, 12
Zamora-Avilés M., Ballesteros-Paredes J., Hartmann L. W., 2017, MNRAS, 472, 647
Zernickel A., Schilke P., Smith R. J., 2013, A&A, 554, L2
Zhang Q., Wang K., Lu X., Jiménez-Serra I., 2015, ApJ, 804, 141

Zhou J.-W. et al., 2021, MNRAS, 508, 4639
Zhou J.-W. et al., 2022, MNRAS, 514, 6038
Zhou J.-W. et al., 2023, MNRAS, 519, 2391

APPENDIX A: EXAMPLES OF N_2H^+(4-3) SPECTRA FITTED WITH SCOUSEPY

Fig. A1 shows a sample of the N_2H^+ (4-3) spectra that are extracted around the local peak in the integrated N_2H^+ emission to the north of MM2 (i.e. location A in Fig. 3). The observed spectra are overlaid with the SCOUSEPY fits obtained following the procedures described in Section 4.1.
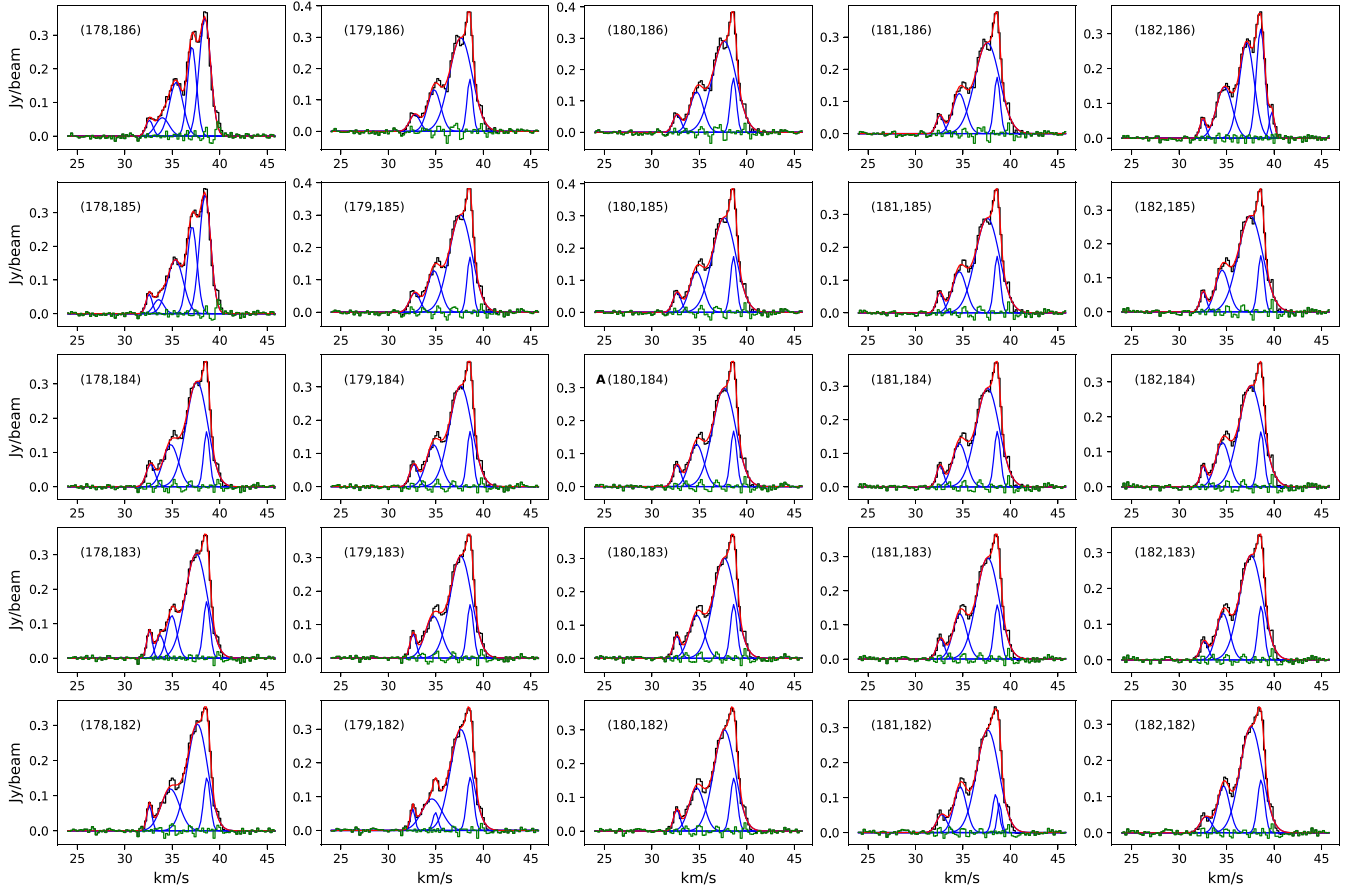
Figure A1. N_2H^+ (4-3) spectra extracted around the local peak in the integrated N_2H^+ emission to the north of MM2 (i.e. location A in Fig. 3). The observed N_2H^+ spectra are shown in black, overlaid with individual best-fitting Gaussian components (blue), total best-fitting models (red), and residuals (green). Each panel is labelled with the pixel coordinates where the spectrum was extracted; the spectrum extracted at location A is additionally labelled with 'A'.

This paper has been typeset from a TEX/LATEX file prepared by the author.